

Tomography-Based Convection and Melt Generation Beneath the Rungwe Volcanic Province, East Africa

Emmanuel A. Njingu¹, D. Sarah Stamps¹, Tyrone O. Rooney², Estella A. Atekwana³, and Tahiry A Rajaonarison¹

¹Virginia Tech

²Michigan State University

³University of Delaware

November 24, 2022

Abstract

Within the Western Branch of the East African Rift (EAR), volcanism is highly localized, which is distinct from the voluminous magmatism seen throughout the Eastern Branch of the EAR. Voluminous magmatism in the Eastern Branch results from plume-lithosphere interactions, but the origin of magmatism in the Western Branch remains enigmatic. Previous investigations of melt generation beneath the Rungwe Volcanic Province (RVP), the southernmost volcanic center in the Western Branch, suggest plume materials are present. Here, we develop a model of tomography-based convection (TBC) with melt generation to test the hypothesis that melt beneath the RVP is sourced from plume materials. To test our hypothesis, we use seismically constrained lithospheric thickness and sublithospheric mantle structure to develop a fully adiabatic 3D thermomechanical model of TBC with melt generation using ASPECT. We test a range of mantle potential temperatures and find values ranging from 1250-1350 °C are unable to generate melt beneath the RVP. However, when the sublithospheric mantle temperature is increased by ~250 K based on constraints from shear wave velocity anomalies, decompression melt generation occurs at a maximum depth of ~150 km beneath the RVP. Our work suggests that excess sublithospheric mantle temperatures are necessary for melt generation beneath the RVP, and that shear wave velocity anomalies can provide a first order estimate of these anomalous mantle conditions. Excess sublithospheric mantle temperature in the RVP suggests the influence of a plume-source for the seismic anomalies and supports existing geochemical interpretations of a mantle plume contribution to magmatism in the RVP.

1 **Tomography-Based Convection and Melt Generation Beneath the Rungwe Volcanic**
2 **Province, East Africa**

3
4 **Emmanuel A. Njinju^{1*}, D. Sarah Stamps¹, Tyrone Rooney², Estella A. Atekwana³, and**
5 **Tahiry A. Rajaonarison⁴**

6
7 ¹Department of Geosciences, Virginia Tech, Blacksburg, VA, USA

8 ²Department of Earth and Environmental Sciences, Michigan State University, East Lansing, MI,
9 USA

10 ³Department of Earth & Planetary Sciences, University of California, Davis, Davis, CA 95616,
11 USA

12 ⁴Institute and Observatory of Geophysics in Antananarivo, University of Antananarivo,
13 Antananarivo, Madagascar

14
15
16
17
18
19
20
21
22 *Corresponding author: Emmanuel A. Njinju (njinju85@vt.edu)

23
24
25 **Keywords:**

- 26 ● Tomography-Based Convection; Melt Generation; Plume Source; Rungwe Volcanic
27 Province; Malawi Rift; East African Rift

28 **Key Points:**

- 29 ● Shear wave tomography constraints suggest excess temperatures of ~250 K beneath the
30 Rungwe Volcanic Province
31 ● Tomography-based convection generates sublithospheric melt beneath the Rungwe
32 Volcanic Province
33 ● Plume material beneath the Rungwe Volcanic Province is consistent with geochemical
34 and seismic observations

35 **Abstract**

36 Within the Western Branch of the East African Rift (EAR), volcanism is highly localized, which
37 is distinct from the voluminous magmatism seen throughout the Eastern Branch of the EAR.
38 Voluminous magmatism in the Eastern Branch results from plume-lithosphere interactions, but
39 the origin of magmatism in the Western Branch remains enigmatic. Previous investigations of
40 melt generation beneath the Rungwe Volcanic Province (RVP), the southernmost volcanic center
41 in the Western Branch, suggest plume materials are present. Here, we develop a model of
42 tomography-based convection (TBC) with melt generation to test the hypothesis that melt
43 beneath the RVP is sourced from plume materials. To test our hypothesis, we use seismically
44 constrained lithospheric thickness and sublithospheric mantle structure to develop a fully
45 adiabatic 3D thermomechanical model of TBC with melt generation using ASPECT. We test a
46 range of mantle potential temperatures and find values ranging from 1250-1350 °C are unable to
47 generate melt beneath the RVP. However, when the sublithospheric mantle temperature is
48 increased by ~250 K based on constraints from shear wave velocity anomalies, decompression
49 melt generation occurs at a maximum depth of ~150 km beneath the RVP. Our work suggests
50 that excess sublithospheric mantle temperatures are necessary for melt generation beneath the
51 RVP, and that shear wave velocity anomalies can provide a first order estimate of these
52 anomalous mantle conditions. Excess sublithospheric mantle temperature in the RVP suggests
53 the influence of a plume-source for the seismic anomalies and supports existing geochemical
54 interpretations of a mantle plume contribution to magmatism in the RVP.

55 **1. Introduction**

56 The presence of thermochemically anomalous plume material within the upper mantle
57 can result in voluminous magmatism, in particular where decompression of this material is

58 facilitated by continental rifting such as in East Africa (e.g., Nielsen & Hopper, 2002; van Wijk
59 et al., 2001; White & McKenzie, 1989). The Eastern Branch of the East African Rift (EAR;
60 Figure 1A) includes widespread magmatism with flood basalts extending hundreds of kilometers.
61 For example, the Kenyan Rift alone in the Eastern Branch has an estimated 924,000 km³ of
62 mafic magma and underplated material generated in the past 30 Ma (Latin et al., 1993). The
63 voluminous magmatism in the Eastern Branch of the EAR originates from thermal perturbations
64 due to plume-lithosphere interactions (e.g., Rogers et al., 2000; MacDonald et al., 2001; Rooney
65 et al., 2012). However, the Western Branch is characterized by limited and sparse magmatism
66 and the source of melt is not well understood (e.g., O'Donnell et al., 2016; Hudgins et al., 2015;
67 Njinju et al., 2021; Rosenthal et al., 2009). Determining the source of melt in the magma-poor
68 Western Branch of the EAR may improve our understanding of the role of melt during the
69 evolution of continental rifting.

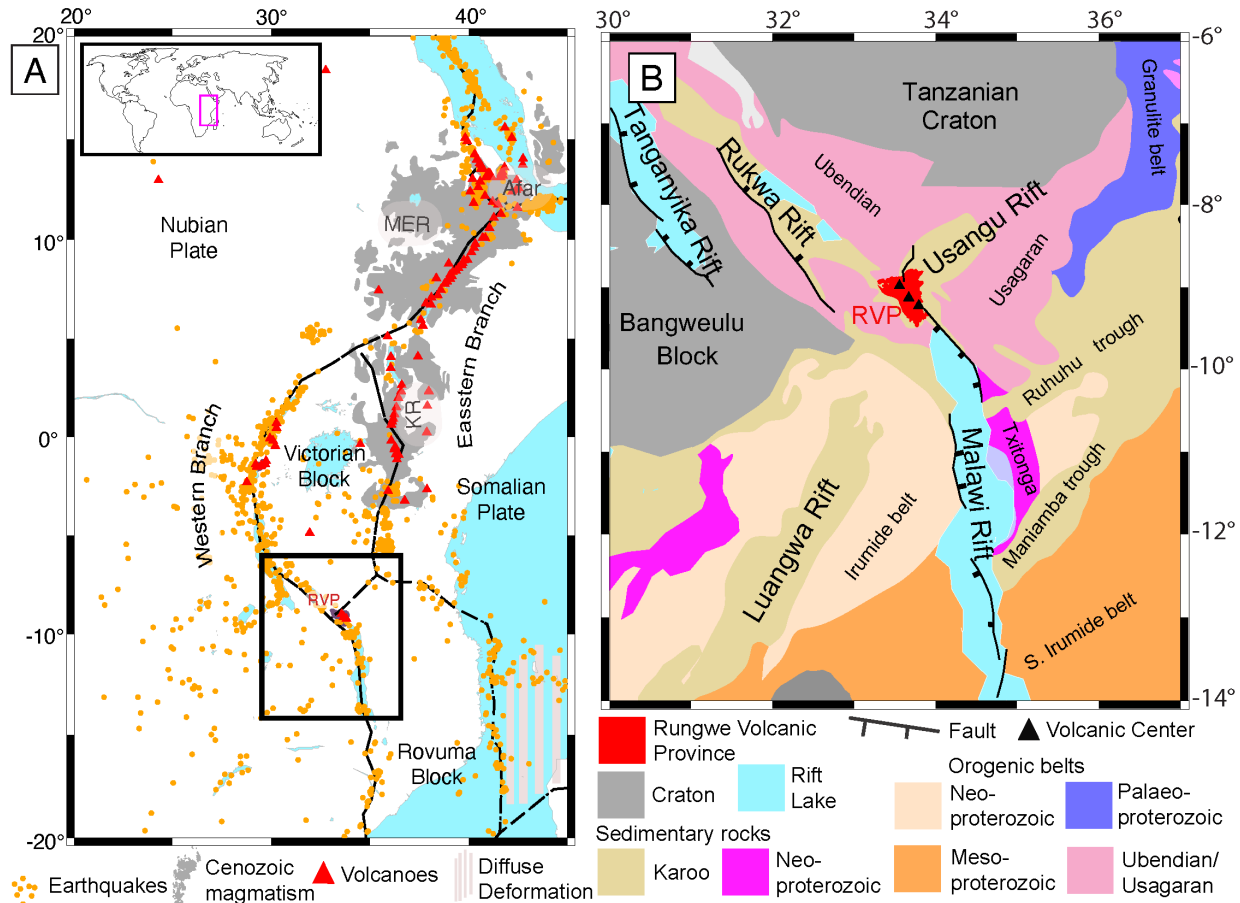
70 The Rungwe Volcanic Province (RVP; Figure 1B) provides a natural laboratory to
71 investigate the source of melt in the magma-poor Western Branch of the EAR. The RVP is the
72 southernmost volcanic center in the Western Branch that lies at the triple junction formed by the
73 Rukwa Rift, Malawi Rift, and the Usangu Rift (Figures 1A and B), which may link the magma-
74 rich Eastern Branch to the Western Branch of the EAR (Purcell, 2018). The RVP lies within the
75 1.8 Ga Ubendian-Usagaran mobile belts that circumvent the thick lithosphere of the Tanzanian
76 and Bangweulu cratons (Figure 1B; e.g., Corti et al., 2007; Fritz et al., 2013; Bahame et al.,
77 2016; Ganbat et al., 2021) and consists of three large volcanoes, Ngozi, Rungwe, and Kyejo that
78 were respectively last active about 1 ka (erupted trachytic tuff), 1.2 ka (erupted trachytic tephra)
79 and 0.2 ka (erupted tephrite lava flow) (Harkin, 1955; Ebinger et al., 1989; Fontijn et al. 2010,
80 2012; black triangles, Figure 1B). Magmatism in the RVP is highly localized with past eruptions

81 covering $\sim 1500 \text{ km}^2$ (Figure 1B; Ebinger et al., 1989, 1997; Fontijn et al., 2012). $^{40}\text{Ar}/^{39}\text{Ar}$
82 radiometric dating of samples from the RVP suggest that magmatism in the RVP started at least
83 by 19 Ma (Mesko et al., 2014; Mesko, 2020) and possibly as early as ~ 25 Ma (Roberts et al.,
84 2012), which predates rifting in the northern Malawi Rift that started at ~ 8.6 Ma (Ebinger et al.,
85 1993) and the reactivation of the Rukwa Rift at ~ 8.7 Ma (Hilbert-Wolf et al., 2017). These ages
86 suggest that magmatism in the RVP might have played an important role in thermally weakening
87 the lithosphere, thereby facilitating rifting, yet the source of the magma beneath the RVP remains
88 enigmatic (i.e., Furman, 1995; Fontijn et al., 2012; Kimani et al., 2021; Njinju et al., 2021).
89 Njinju et al. (2021) tested a non-plume hypothesis for the source of the melt beneath the RVP by
90 developing a 3D regional thermomechanical model of passive upwelling driven by lithospheric
91 modulated convection (LMC) and constrained the parameters required for sublithospheric melt
92 generation due to LMC. The model by Njinju et al. (2021) is unable to generate melt except for
93 cases that have elevated mantle potential temperatures ($T_p \geq 1800 \text{ K}$), which suggests an
94 anomalous heat source consistent with existing geochemical interpretations (Rooney et al.,
95 2012).

96 The aim of this study is to investigate the source of melt beneath the RVP by testing the
97 hypothesis that the melt beneath the RVP is sourced from mantle plume materials, which can be
98 constrained by shear wave seismic velocities using a model of tomography-based convection
99 (TBC). Here, we develop a 3D thermomechanical model of TBC and melt generation beneath the
100 RVP using the finite element code ASPECT (Advanced Solver for Problems in Earth's
101 ConvecTion; Bangerth et al., 2018a; Bangerth et al., 2018b; Heister et al., 2017; Dannberg &
102 Heister, 2016). TBC is defined as a model of mantle convection that is generated from
103 temperature variations derived from seismic velocity perturbations. We impose a laterally

104 varying rigid lithosphere (Fishwick, 2010) with an approximately conductive geotherm that is
105 modeled as a linear gradient from the surface (293 K) to the base of the lithosphere (T_{LAB} ;
106 temperature at lithosphere-asthenosphere boundary), which is an adiabatic boundary defined by
107 T_p (McKenzie and Bickle, 1988). For the sublithospheric mantle, we implement a fully adiabatic
108 initial temperature condition with additional temperature perturbations derived from shear wave
109 seismic velocity constraints from Emry et al. (2019). We also use rheological flow laws that
110 account for melt generation in a continental setting following Njinju et al. (2021).

111 We find upwelling asthenosphere from TBC beneath the RVP where the lithosphere is
112 relatively thin and slow seismic velocity anomalies are present. This work builds upon our
113 previous study (Njinju et al., 2021), which suggests that asthenospheric upwelling arising from
114 ambient mantle potential temperature is unable to generate melt beneath the RVP. Here, our
115 results show that with a seismically derived excess temperature of ~ 250 K beneath the RVP,
116 upwelling from TBC generates decompression melt at a maximum depth of ~ 150 km beneath the
117 RVP. Since the seismically-derived excess temperature is consistent with the temperature range
118 for mantle plumes (200 – 300 K, i.e., McKenzie and O’Nions, 1991; Watson and McKenzie,
119 1991; Schilling, 1991; Herzberg and O’Hara, 2002; Herzberg et al., 2007; Putirka, 2008), we
120 suggest that plume materials are necessary for melt generation beneath the RVP, consistent with
121 existing geochemical interpretations (Hilton et al., 2011; Furman, 2007; Castillo et al., 2014).



122

123 **Figure 1. (A).** Map of the East African Rift (EAR) showing the Eastern and Western Branches.
 124 The Western Branch of the EAR has fewer volcanic centers (red triangles are Holocene
 125 volcanoes) and more earthquakes (orange dots are earthquakes with >M2) than the Eastern
 126 Branch. The Holocene volcanoes are from the Smithsonian Global Volcanism Project and the
 127 earthquakes are from the NEIC catalog (Beauval et al., 2013). The Cenozoic volcanic rocks
 128 (gray) are outlined after Thiéblemont (2016) and indicate the large igneous province in East
 129 Africa. RVP = Rungwe Volcanic Province. KR = Kenyan Rift. MER = Main Ethiopian Rift. The
 130 black rectangle shows the location of Figure 1B. Dashed lines represent plate boundaries from
 131 Stamps et al. (2008). RVP lies at the Mbeya triple junction. The diffuse deformation offshore of the
 132 Eastern Branch is based on a geodetic study by Stamps et al. (2021). **(B).** Map of major terranes
 133 and geological features in the southern part of the Western Branch of the EAR that are based on
 134 Fritz et al. (2013). The major rift faults are extracted from Muirhead et al. (2019). Black triangles
 135 from north to south represent the three large active volcanoes (Ngozi, Rungwe and Kyejo;
 136 Fontijn et al., 2010; Harkin, 1960) of the RVP.
 137

138 **2. Methods**

139 We model time-dependent TBC in a 3D regional domain that incorporates melt
 140 generation in the sublithospheric mantle using the finite element code ASPECT (Bangerth et al.,
 141 2018a; Bangerth et al., 2018b; Heister et al., 2017; Dannberg & Heister, 2016) to test the
 142 hypothesis that the melt beneath the RVP is sourced from mantle plume materials that can be
 143 constrained by seismic velocity perturbations.

144 2.1. 3D Tomography-Based Convection Modeling

145 2.1.1. Governing Equations

146 We apply the anelastic liquid approximation (Jarvis & McKenzie, 1980) for compressible
 147 fluid flow to calculate TBC beneath the RVP. The anelastic liquid approximation is based on two
 148 assumptions. The first assumption is that lateral density variations relative to a reference density
 149 profile $\bar{\rho}(\bar{p}, \bar{T})$ are small and can be accurately described by a Taylor expansion. i.e.:

$$150 \quad \rho(p, T) \approx \bar{\rho}(\bar{p}, \bar{T}) + \frac{\partial \bar{\rho}(\bar{p}, \bar{T})}{\partial p} p' + \frac{\partial \bar{\rho}(\bar{p}, \bar{T})}{\partial T} T' \quad (1)$$

151 where $p' = p - \bar{p}$ and $T' = T - \bar{T}$ are, respectively, perturbations of the pressure (p) and
 152 temperature (T) relative to the reference pressure profile (\bar{p}) and the reference temperature
 153 profile \bar{T} . \bar{T} and \bar{p} are defined by the adiabatic conditions below:

$$154 \quad \frac{d\bar{T}}{dz} = \frac{\alpha \bar{T} \mathbf{g}}{C_p} \quad (2)$$

$$155 \quad \frac{d\bar{p}}{dz} = \bar{\rho} \cdot \mathbf{g} \quad (3)$$

156

157 where α , \mathbf{g} , C_p is, respectively the thermal expansivity, gravitational acceleration and specific
 158 heat. Thermal expansivity is defined as $\alpha = -\frac{1}{\bar{\rho}} \frac{\partial \bar{\rho}(\bar{p}, \bar{T})}{\partial T}$ and, isothermal compressibility is
 159 defined as $\beta = \frac{1}{\bar{\rho}} \frac{\partial \bar{\rho}(\bar{p}, \bar{T})}{\partial p}$. Thus in terms of α and β , Eq. 1 becomes:

$$160 \quad \rho(p, T) \approx \bar{\rho}(1 - \alpha(T - \bar{T}) + \beta(p - \bar{p})) \quad (4a)$$

161 and the density perturbation,

$$162 \quad \rho(p, T) - \bar{\rho}(\bar{p}, \bar{T}) \approx -\alpha \bar{\rho}(T - \bar{T}) + \beta \bar{\rho}(p - \bar{p}) \quad (4b)$$

163 The second assumption in the anelastic liquid approximation is that variations in density
 164 from the reference density can be neglected in the mass and energy conservation equations and
 165 are only considered in the buoyancy term (right-hand side of the momentum equation, Eq. 5;
 166 Gassmüller et al., 2020) which describes the main driving force of the flow. With the anelastic
 167 liquid approximation, the conservation equations of momentum (Eq. 5) and mass (Eq. 6) are
 168 given by:

$$169 \quad -\nabla \cdot \left[2\eta \boldsymbol{\varepsilon}(\mathbf{u}) - \frac{1}{3}(\nabla \cdot \mathbf{u})\mathbf{1} \right] + \nabla p' = (-\alpha \bar{\rho}(T - \bar{T}) + \beta \bar{\rho}(p - \bar{p}))\mathbf{g} \quad \text{in } \Omega, \quad (5)$$

$$170 \quad \nabla \cdot \bar{\rho}\mathbf{u} = 0 \quad \text{in } \Omega, \quad (6)$$

171 where $\boldsymbol{\varepsilon}(\mathbf{u})$ and η are, respectively, the strain rate and viscosity. We model the TBC by solving
 172 for the velocity, \mathbf{u} , in Eq. 5 and Eq. 6.

173 In order to model melt generation, we also simulate changes in temperature due to heat
 174 transfer in the model by solving for temperature T in the energy conservation equation (Eq. 7).
 175 The formulation of anelastic liquid approximation checks that shear heating (first term in the
 176 right-hand side of Eq. 7) and adiabatic heating (second term in the right-hand side of Eq. 7) are
 177 included in the heating model. We simplify the adiabatic heating term by using the hydrostatic

178 pressure gradient (Eq. 3). Since we are modeling melt generation, we include the latent heat of
 179 melting (third term in the right-hand side of Eq. 7) in the heating model:

$$\begin{aligned}
 180 \quad \bar{\rho} C_p \left(\frac{\partial T}{\partial t} + \mathbf{u} \cdot \nabla T \right) - \nabla \cdot k \nabla T &= 2\eta \left(\varepsilon(\mathbf{u}) - \frac{1}{3}(\nabla \cdot \mathbf{u})\mathbf{1} \right) : \left(\varepsilon(\mathbf{u}) - \frac{1}{3}(\nabla \cdot \mathbf{u})\mathbf{1} \right) \\
 181 \quad &+ \alpha \bar{\rho} T (\mathbf{u} \cdot \mathbf{g}) \quad (7) \\
 182 \quad &+ \bar{\rho} T \Delta S \left(\frac{\partial F}{\partial t} + \mathbf{u} \cdot \nabla F \right) \quad \text{in } \Omega,
 \end{aligned}$$

183 We assume a uniform crustal thickness of 30 km in the model with an average thermal
 184 conductivity of $k = 2.5 \text{ W.m}^{-1} \cdot \text{K}^{-1}$ (Njinju et al., 2019a) and a uniform reference density of 2700
 185 kg/m^3 for the crustal domain. For the lithospheric mantle, we assume an average thermal
 186 conductivity of $3.5 \text{ W.m}^{-1} \cdot \text{K}^{-1}$ (Burov, 2011; Koptev et al., 2018) and a uniform reference
 187 density of 3300 kg/m^3 . We define a thermal conductivity of $4.7 \text{ W.m}^{-1} \cdot \text{K}^{-1}$ for the
 188 sublithospheric mantle (Clauser & Huenges, 1995; Dannberg & Heister, 2016; Dannberg et al.,
 189 2019). We consider melt buoyancy in the sublithospheric mantle by assuming a reference density
 190 defined by the effective density of partially molten rocks (ρ_{eff}), i.e.:

$$191 \quad \rho_{eff} = \bar{\rho} = \rho_{solid} - F(\rho_{solid} - \rho_{melt}) \quad (8)$$

192 where F is the melt fraction (see section 2.2 below), the densities of solid rock $\rho_{solid} = 3300$
 193 kg/m^3 and the density of melt $\rho_{melt} = 3000 \text{ kg/m}^3$.

194 Our model extends to 660 km depth, but we do not model phase changes in the mantle
 195 transition zone since our focus is on shallow asthenospheric melt generation. For the Earth's
 196 sublithospheric mantle we define $\alpha = 3 \times 10^{-5} \text{ K}^{-1}$, $C_p = 1250 \text{ J.kg}^{-1} \cdot \text{K}^{-1}$, and $\beta = 4.2 \times 10^{-12} \text{ Pa}^{-1}$
 197 following Dannberg and Heister (2016). The latent heat consumed during melting is proportional
 198 to the melting rate $\Gamma = \bar{\rho} \left(\frac{\partial F}{\partial t} + \mathbf{u} \cdot \nabla F \right)$ and the entropy change ΔS (Eq. 7). The latent heat of

199 melting is incorporated with an entropy change of $\Delta S = -300 \text{ J.kg}^{-1} \cdot \text{K}^{-1}$ also following Dannberg
 200 and Heister (2016).

201 2.1.2. Model Setup

202 We use seismically constrained lithospheric structure (Figure 2A; Fishwick, 2010) and
 203 shear wave velocity perturbations in the sublithospheric mantle (Figure 2B; Emry et al., 2019) to
 204 define the initial temperature field of the model. The lithosphere is thinnest beneath the RVP
 205 ($\sim 100 - 120 \text{ km}$) and thickest beneath the central to southern segment of the Malawi Rift ($\sim 175 -$
 206 200 km). This is consistent with gravity derived lithospheric depth estimates in Njinju et al.
 207 (2019a). We assume an approximately conductive geothermal temperature distribution for the
 208 lithosphere by implementing a linear temperature gradient from the surface ($T_0 = 293 \text{ K}$) to the
 209 base of the lithosphere (T_{LAB}), which is an adiabatic boundary defined by the T_p (Eq. 9 derived
 210 from the adiabatic temperature gradient $\left(\frac{\partial T}{\partial z}\right)_s = \frac{\alpha T g}{C_p}$; Mckenzie and Bickle, 1988).

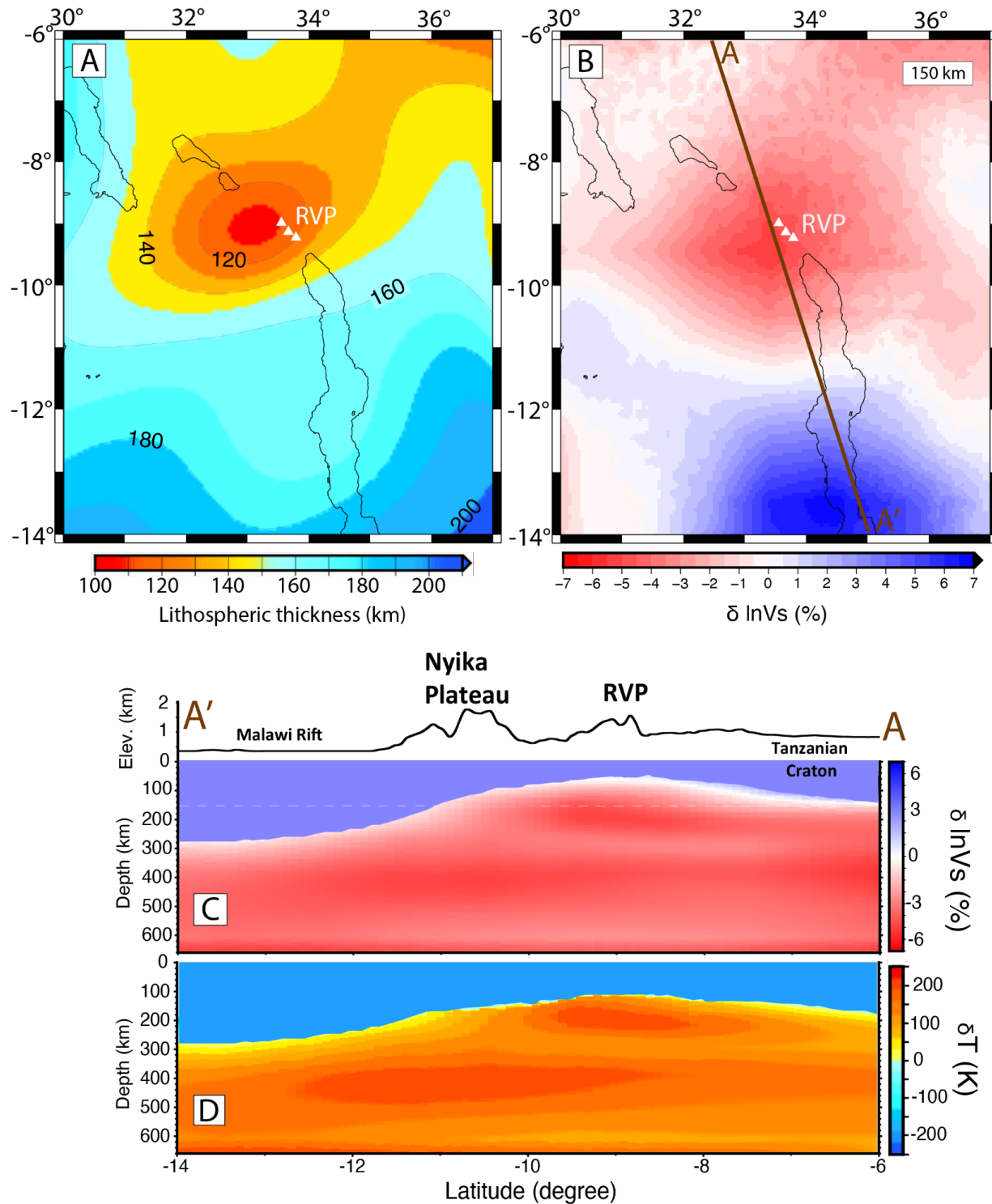
$$211 \quad T_{LAB} = T_p * e^{\left[\frac{g \alpha z_{LAB}}{C_p}\right]} \quad (9)$$

212 where g , α , z_{LAB} and C_p is, respectively, the gravitational acceleration, thermal expansivity,
 213 depth to the lithosphere-asthenosphere boundary (LAB), and specific heat. We test a wide range
 214 of mantle potential temperatures ($T_p = \sim 1250 - 1475 \text{ }^\circ\text{C}$; $1523 - 1748 \text{ K}$; see section 3.1 below).
 215 The variable lithospheric structure (Figure 2A; Fishwick, 2010) produces lateral variations in
 216 temperature and pressure, which leads to lateral density perturbations in the sublithospheric
 217 mantle. The initial temperature of the sublithospheric mantle (T_{SLM}) consists of a background
 218 temperature (T_{SLB}) that increases adiabatically to the base of the model (Eq. 10a; McKenzie &
 219 Bickle, 1988) with an additional temperature perturbation derived from shear wave velocity

220 anomalies (Eq. 10b; Figures 2B and 2C; Emry et al., 2019). We first convert the shear wave
221 velocity anomalies $\delta v_s/v_s$ from Emry et al. (2019) to the equivalent density perturbations $\delta\rho/\rho$
222 using a velocity-density conversion factor of 0.15 (Becker, 2006; Conrad & Lithgow-Bertelloni,
223 2006, Conrad and Behn, 2010), using Eq.10a. We follow the approach of Austermann et al.
224 (2017) and multiply the derived density perturbations to the negative inverse of thermal
225 expansivity α to obtain the temperature anomaly δT (Eq. 10b; Figure 2D).

$$226 \quad \delta \ln \rho = \frac{\delta \rho}{\rho} = 0.15 * \delta \ln v_s = 0.15 * \frac{\delta v_s}{v_s} \quad (10a)$$

$$227 \quad \delta T = -\frac{1}{\alpha} * \delta \ln \rho \quad (10b)$$



228

229 **Figure 2.** (A) Lithospheric thickness map of the Rungwe Volcanic Province (RVP, white
 230 triangles) and surroundings, updated from Fishwick (2010), which we use as input in this study.
 231 Contours show lines of equal lithospheric thickness at 20 km intervals. The thinnest lithosphere
 232 (~100 km) adjacent to RVP occurs beneath the Mbeya triple junction. Black lines indicate the

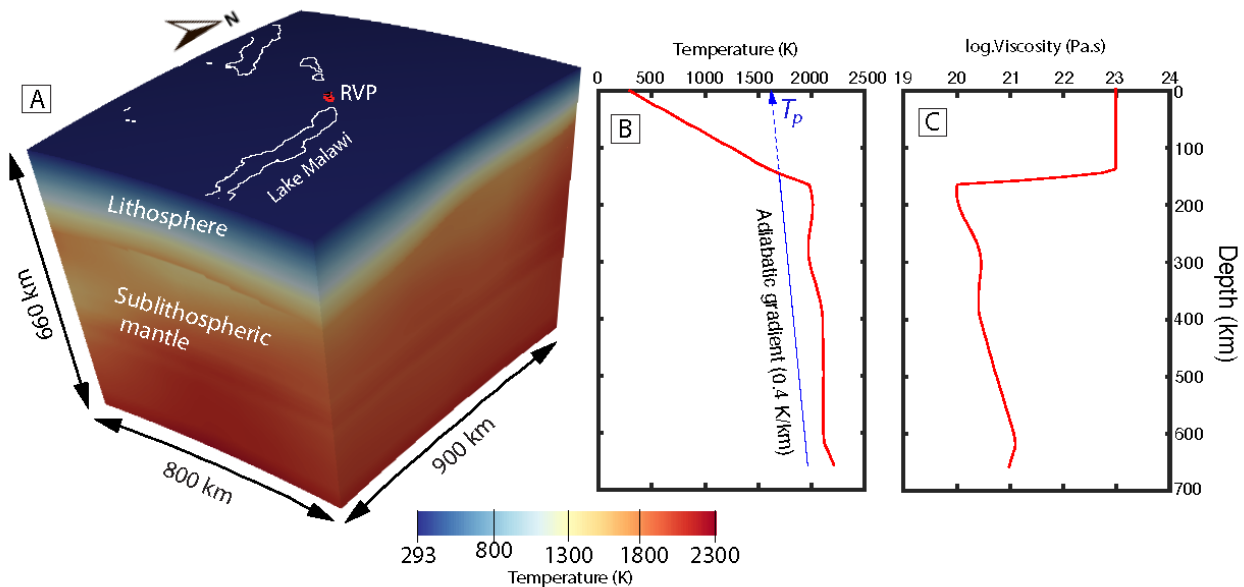
233 outline of rift lakes. **(B)** 150 km depth slice of seismic velocity perturbation derived from Emry
 234 et al. (2019). The velocities are relative to the AK135 global average Earth Model (Kennett et al.,
 235 1995). Brown line AA' is the profile location for Figures 2C and D. **(C)** Cross section of seismic
 236 velocity perturbation after Emry et al. (2019) along profile AA'. The velocities are relative to the
 237 AK135 global average Earth Model (Kennett et al., 1995). **(D)** Temperature anomalies derived
 238 from the velocity perturbations in Figure 2C.
 239

$$240 \quad T_{SLB} = T_p * e^{\left[\frac{g\alpha z}{C_p}\right]} \quad (11a)$$

$$241 \quad T_{SLM} = T_{SLB} + \delta T \quad (11b)$$

242 where the sublithospheric depth, $z > z_{LAB}$ (depth to LAB). T_{SLB} , T_{SLM} , g , α and C_p is, respectively,
 243 the background temperature in the sublithospheric mantle, the temperature in the sublithospheric
 244 mantle, the gravitational acceleration, thermal expansivity and specific heat. The resultant initial
 245 temperature structure is shown in Figures 3A and 3B.

246



247

248 **Figure 3.** (A) Numerical model setup showing the model dimensions and the initial temperature
 249 condition as the background in 3D. Red triangles represent the RVP. White lines show the
 250 outline of rift lakes. (B) Initial temperature-depth profile beneath the RVP (red line). Blue line
 251 represents the 0.4 K/km adiabat for reference. T_p = mantle potential temperature. (C) Initial
 252 viscosity-depth profile beneath the RVP (red line).

253

254

255

256

257

258

259

260

261

262

Our model domain has dimensions of 800 x 900 x 660 km along latitude, longitude, and depth, respectively, for a spherical chunk geometry (Figure 3A). We refine the entire model domain to a global mesh refinement of 6 such that each element is $\sim 12 \times 14 \times 10$ km with 17.5 million unknowns computed on 640 processors. We set the velocities at all sides of the model to zero, which exerts minimal edge-effects on the model interior from the boundaries of the model as shown in Njinju et al. (2019a, b). The temperature boundary conditions are given by fixed temperatures at the surface and bottom of the model with zero heat flux at the sides of the model (e.g., Rajaonarison et al., 2020). The surface temperature is fixed at 293 K while the temperature at the base of the model is defined by the temperature in Eq. 11b for $z = 660$ km.

263

2.1.3. Rheology

264

265

266

267

268

269

270

271

We impose a strong, uniform viscosity of 10^{23} Pa.s for the lithosphere (Figure 3C), while for the sublithospheric mantle we use non-Newtonian, temperature-, pressure- and porosity-dependent creep laws of anhydrous peridotite. The viscosity of the sublithospheric mantle (η_{SLM}) is given by the multiplication of a porosity dependence factor to a background viscosity governed by the composite rheology of dry olivine material parameters following Rajaonarison et al. (2020). The composite rheology (η_{comp}) is the harmonic average of the viscosity from dislocation-creep (η_{disl}) and diffusion-creep (η_{diff}) flow laws of dry olivine (Jadamec & Billen, 2010):

272

$$\eta_{diff, disl} = \frac{1}{2} A \frac{1}{n} d^{\frac{m}{n}} \dot{\epsilon}^{\frac{1-n}{n}} \exp\left(\frac{E_a + pV_a}{nRT}\right) \quad (12a)$$

273

$$\eta_{comp} = \frac{\eta_{diff} \times \eta_{disl}}{\eta_{diff} + \eta_{disl}} \quad (12b)$$

$$\eta_{SLM} = \eta_{comp} \times e^{[-\alpha\phi\phi]} \quad (12c)$$

274
 275 where A is the prefactor, n is the stress exponent, $\dot{\epsilon}$ is the square root of the second invariant of
 276 the deviatoric strain rate tensor, d is the grain size, m is the grain size exponent, E_a is the
 277 activation energy, V_a is the activation volume, p is pressure, R is the gas constant, and T is the
 278 temperature. The values for the parameters A , n , m , E_a and V_a are obtained from experimental
 279 studies of dry olivine (Hirth & Kohlstedt, 2004; Table 1). The exponential melt-weakening factor
 280 is experimentally constrained to $25 \leq \alpha\phi \leq 30$ (Mei et al., 2002). We use $\alpha\phi = 27$ following
 281 Dannberg and Heister (2016). The porosity Φ is the ratio of the volume of pore spaces between
 282 the olivine grains of peridotite to the bulk volume of the peridotite constituent of the
 283 asthenosphere. The material properties for each layer (lithosphere and sublithospheric mantle)
 284 are tracked through compositional fields with the asthenosphere and transition zone further
 285 divided into two compositional fields called “porosity” and “peridotite”. Partial melt in the
 286 model is tracked through the compositional field “porosity”. The viscosity at each quadrature
 287 point is calculated from the harmonic average of the compositional fields weighted by the
 288 volume fraction of each composition at the same location.

289

Table 1. Rheological Parameters for Dry Olivine Used in the Viscosity Flow Law of the
 Sublithospheric Mantle

Parameter	Symbol	Dislocation creep	Diffusion creep	Unit
Activation energy	E_a	530×10^3	$375 \pm 50 \times 10^3$	J/mol
Activation volume	V_a	25×10^{-6}	6×10^{-6}	m ³ /mol

Grain size	d	-	10×10^{-3}	m
Grain size exponent	m	-	3	-
Stress exponent	n	3.5	1.0	-
Prefactor	A	7.4×10^{-15}	4.5×10^{-15}	$\text{Pa}^{-n}\text{m}^m\text{s}^{-1}$

The rheological parameters for the sublithospheric mantle are from Hirth & Kohlstedt (2004). The prefactor in Hirth & Kohlstedt (2004) (i.e., A') is derived from uniaxial strain experiments and is converted to the plane strain equivalent (i.e., A) using the following relationship: $A = \frac{n+1}{2^{l-n}} \times 10^{-6(m+n)} A'$ for dry olivine (Becker, 2006).

290

291 2.2. Partial Melting

292 We model low extent batch melting of anhydrous lherzolite, which occurs prior to the
293 exhaustion of clinopyroxene. Batch melting is considered melting of an upwelling parcel of
294 mantle rock without instantaneous melt extraction and assumes that the melt fraction only
295 depends on temperature, pressure, and how much melt has already been generated at a given
296 point (Ribe, 1985; Asimow & Stolper, 1999). Like the LMC modeling by Njinju et al. (2021),
297 we do not model melt extraction by two-phase flow. However, we mimic melt extraction by
298 switching off the latent heat release during melt freezing. This is done by setting the melt
299 freezing rate to zero such that the latent heat term in Eq. 7 turns off once the melting rate $\Gamma =$
300 $\bar{\rho} \left(\frac{\partial F}{\partial t} + \mathbf{u} \cdot \nabla F \right)$ (Eq. 7) becomes negative due to downwelling and resultant cooling in the
301 melting region. We simulate convection and batch melting for 20 Ma to ensure that steady state
302 is achieved.

303 We use the melting parameterization by Katz et al. (2003), which is valid for shallow
 304 upper mantle melting beneath continental lithosphere at pressures generally less than 13 GPa.
 305 Partial melting in the sublithospheric mantle occurs if the T_p is such that an adiabatically
 306 ascending mantle intersects the solidus (Figure 4; McKenzie & Bickle, 1988). The derived melt
 307 fraction $F(p, T)$ depends on the pressure p (Pa) and temperature T (K) and is given by:

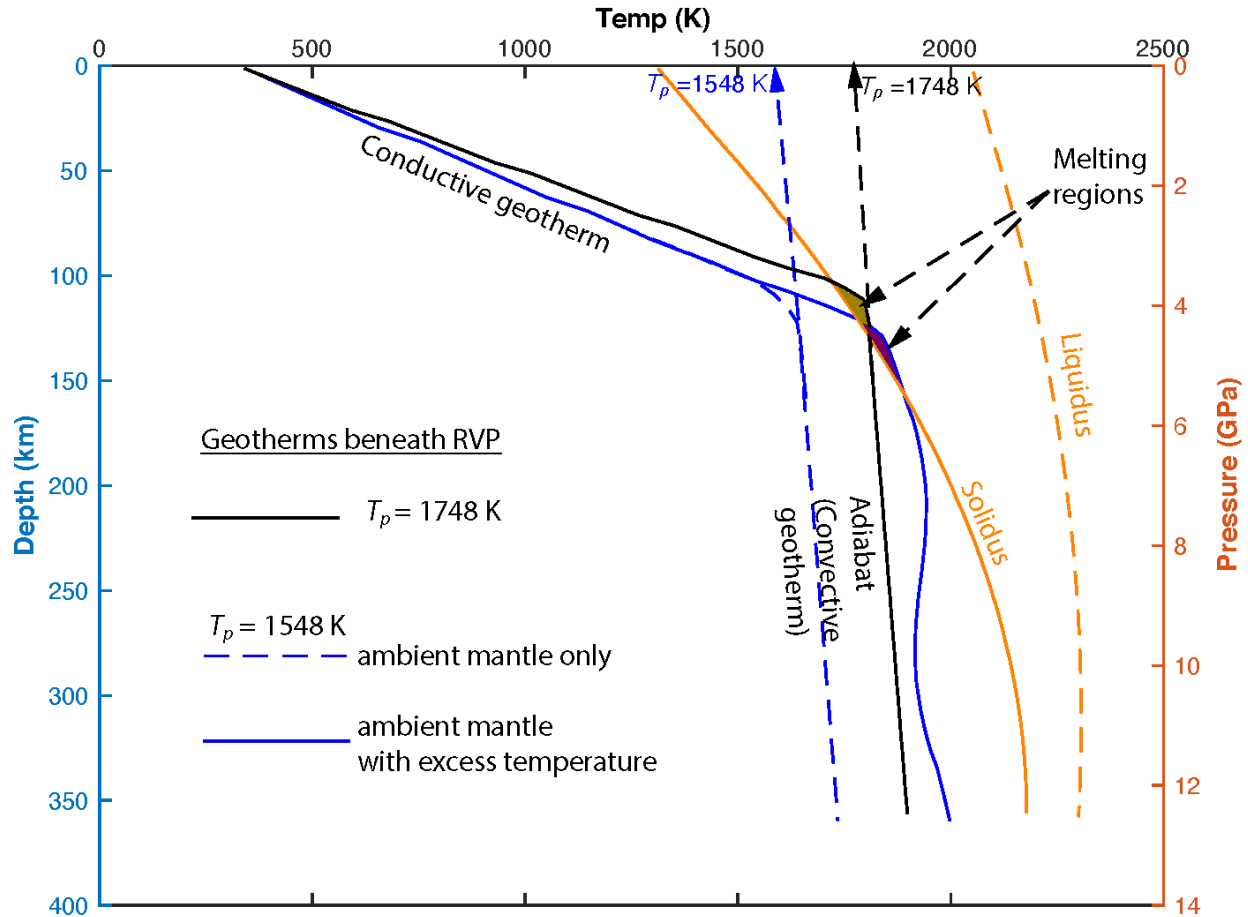
$$308 \quad F(p, T) = \left(\frac{T - T_{solidus}}{T_{liquidus} - T_{solidus}} \right)^{1.5} \quad \text{for} \quad T_{solidus} \leq T \leq T_{liquidus} \quad (13a)$$

309
 310 where the mantle solidus temperature $T_{solidus}$ and liquidus temperature $T_{liquidus}$ are respectively
 311 given by:

$$312 \quad T_{solidus} = A_1 + A_2 p + A_3 p^2 \quad (13b)$$

$$313 \quad T_{liquidus} = B_1 + B_2 p + B_3 p^2 \quad (13c)$$

314
 315
 316 where $A_1 = 1085.7$ °C, $A_2 = 1.329 \times 10^{-7}$ °C/Pa, $A_3 = -5.1 \times 10^{-18}$ °C/Pa², $B_1 = 1475.0$ °C, $B_2 = 8.0$
 317 $\times 10^{-8}$ °C/Pa, and $B_3 = -3.2 \times 10^{-18}$ °C/Pa².



318

319 **Figure 4.** A combined plot of temperature-depth profiles and a pressure-temperature phase
 320 diagram depicting shallow melting of anhydrous peridotite parameterized from Katz et al.
 321 (2003). Blue-dashed lines represent the geotherm for an ambient mantle (constrained with $T_p =$
 322 1548 K) beneath the RVP. Blue solid line is the geotherm when a tomography-based (Emry et
 323 al., 2019) excess temperature is added to the ambient mantle temperature. Black solid line
 324 represents the geotherm beneath the RVP constrained with $T_p = 1748$ K. The orange solid line
 325 represents the solidus (0% melt), and the orange-dashed line represents the liquidus (100% melt).
 326 The solidus and liquidus are plotted from equations (13b) and (13c) respectively. T_p represents
 327 the mantle potential temperature.
 328

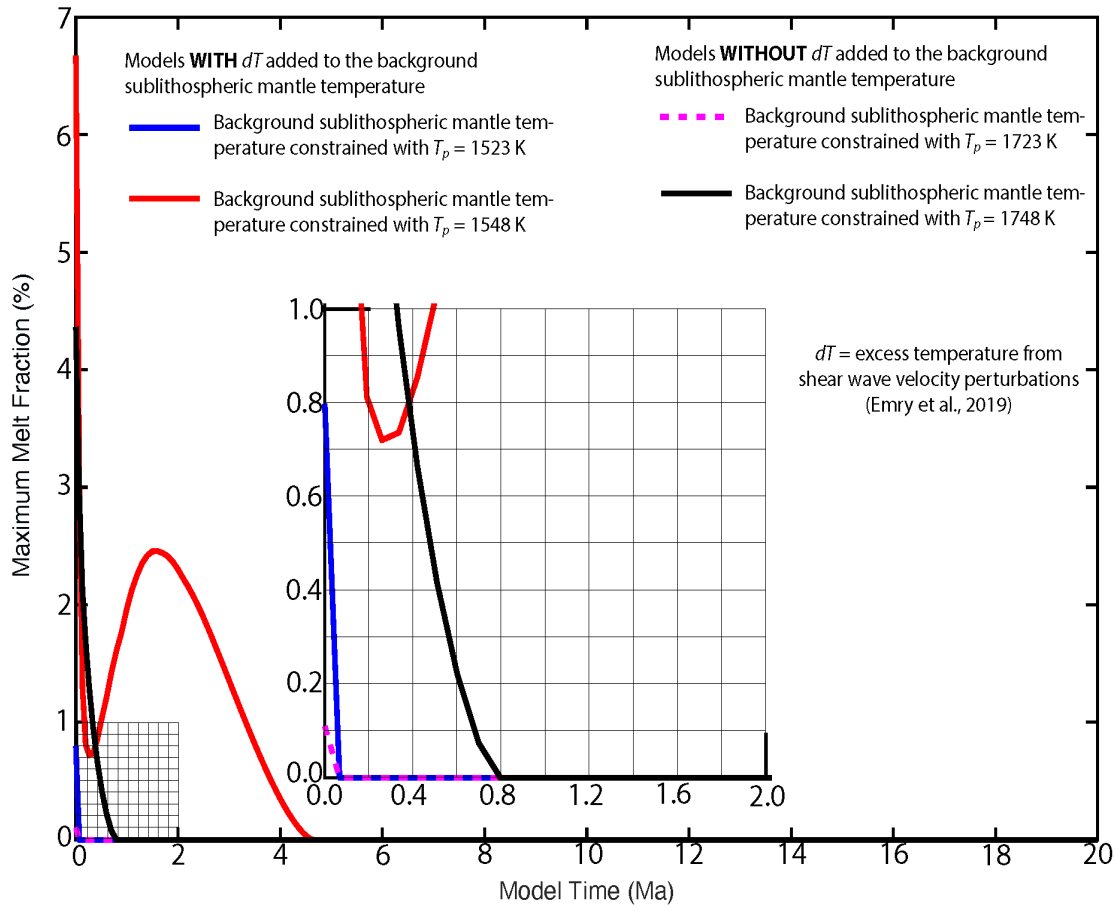
329 3. Results

330 3.1. Tests of Mantle Potential Temperatures and the Effect of Excess Sublithospheric Mantle 331 Temperature in Melt Generation

332 3.1.1. Sensitivity Tests of Mantle Potential Temperature in Melt Generation

333 Partial melting in the sublithospheric mantle occurs if the mantle potential temperature
334 T_p , is such that an adiabatically ascending mantle intersects the solidus (Figure 4; i.e., Njinju et
335 al., 2021). The derived melt fraction is proportional to the temperature in excess of the solidus.
336 Adiabatically rising mantle with higher T_p (e.g., $T_p = 1748$ K, black line; Figure 4) is more likely
337 to intersect the solidus than adiabatically rising mantle with lower T_p (e.g., 1548 K, blue dashed
338 line; Figure 4). Therefore, partial melting in the sublithospheric mantle is highly dependent on T_p
339 . Geochemical observations from the RVP suggest that the T_p in the RVP is elevated and ranges
340 from ~ 1420 - 1450 °C ($\sim 1693 - 1723$ K; Rooney et al., 2012). However, more recent temperature
341 estimates of olivine thermobarometry from volcanic samples from the RVP range from 1199-
342 1375 °C ($1472 - 1648$ K; Class et al., 2018; Mesko, 2020). These may not represent T_p in the
343 sublithospheric mantle if they are from samples of solidified magma. However, according to
344 Faul and Jackson (2005) and Goes et al. (2012), who applied empirical relationships to model
345 mantle material properties, the temperature range of 1199- 1375 °C is a reasonable range for
346 normal ambient asthenosphere. We therefore test a wide range of mantle potential temperatures
347 beneath the RVP ($T_p = \sim 1250$ - 1475 °C; $1523 - 1748$ K). The geotherms for $T_p = 1523 - 1548$ K
348 do not intersect the solidus (for example, dashed blue lines; Figure 4) and so there is no
349 decompression melt even after running the model for 20 Ma. For $T_p = 1723$ K (1450 °C), the
350 geotherm crosses the solidus producing an instantaneous decompression melt with melt fraction
351 of 0.1% (purple lines, Figure 5). We further test a higher T_p value, that is, $T_p = 1748$ K (1475 °C)
352 and observe that the geotherm crosses the solidus producing an initial decompression melt with
353 melt fraction of ~ 4.3 % (black lines, Figure 5), which decreases rapidly and ceases before 0.8
354 Ma. The transient behavior of our melting model is likely due to a transient phase of adiabatic
355 cooling while convection reaches steady state (Njinju et al., 2021). This test demonstrates that in

356 order to generate decompression melt beneath the RVP, the mantle potential temperature must be
 357 elevated ($T_p \geq 1723$ K) suggesting a heat source at depth.



358

359 **Figure 5.** Sensitivity tests of mantle potential temperature and the effect of excess
 360 sublithospheric mantle temperature in melt generation. A plot of maximum melt fraction versus
 361 model time showing the evolution of melt in the model for different sublithospheric mantle
 362 temperature conditions. Models with ambient sublithospheric mantle temperatures constrained
 363 with $T_p = 1523$ K and $T_p = 1548$ K, that is, without tomography-based (Emry et al., 2019) excess
 364 temperatures generate no melt and so are not indicated. The gridded region is zoomed-in for
 365 better visibility and shown as an inset.

366

367 3.1.2 Test of the Effect of Excess Sublithospheric Mantle Temperature in Melt Generation

368

We examine a deep heat source by testing the effect of tomography-based (Emry et al.,

369

2019) excess sublithospheric mantle temperature in melt generation beneath the RVP. No melt is

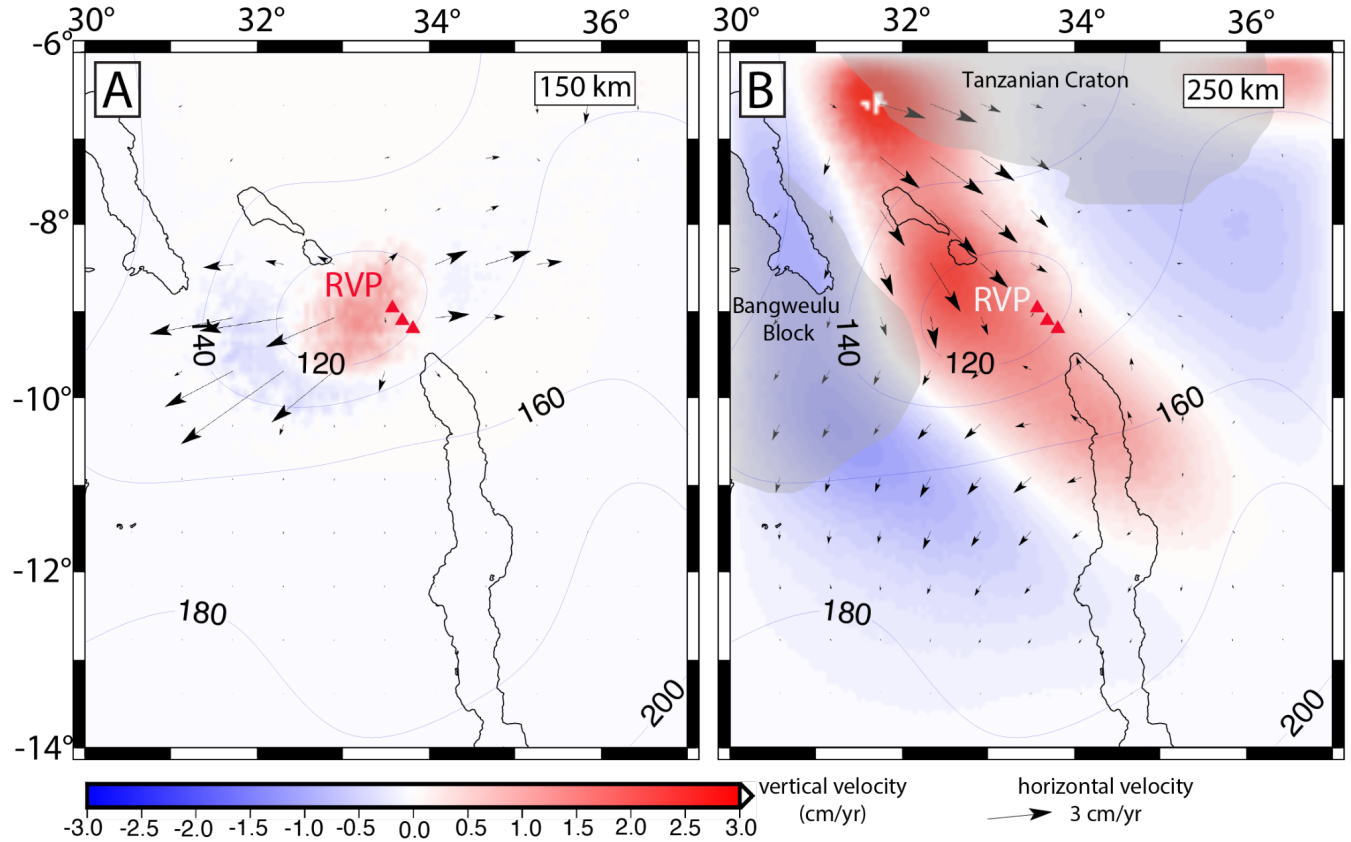
370 generated for ambient sublithospheric mantle conditions beneath the RVP ($T_p = 1523\text{-}1548$ K).
371 But adding the tomography-based excess temperature to the background mantle temperature that
372 is constrained with $T_p = 1523\text{-}1548$ K, leads to geotherms hot enough to intersect the solidus (see
373 solid blue line in Figure 4 for $T_p = 1548$ K) thereby generating decompression melts. For ambient
374 sublithospheric mantle conditions constrained with $T_p = 1523$ K, adding the tomography-based
375 excess temperature generates an instantaneous decompression melt with a melt fraction of 0.79
376 % (blue solid lines, Figure 5). For ambient sublithospheric mantle conditions constrained with T_p
377 = 1548 K, adding the tomography-based excess temperature (red lines, Figure 5), generates an
378 initial decompression melt with melt fraction of ~ 6.6 % (red lines, Figure 5) beneath the RVP.
379 With the tomography-based excess temperature, the initial geotherm is hot enough such that as
380 the model evolves to steady state, TBC generates the second stage of decompression melting
381 when the adiabatic gradients within the active convection cell adjust from the initial values. This
382 test demonstrates that for ambient sublithospheric mantle conditions constrained with $T_p = 1548$
383 K, TBC can generate decompression melt beneath the RVP if the excess temperature ≤ 250 K.

384 3.2 Tomography-Based Convection

385 In our numerical model, TBC in the sublithospheric mantle arises from our initial
386 temperature conditions. The lithosphere, which is made rigid in the model by imposing a high
387 viscosity (10^{23} Pa.s), is not deforming. We assume a rigid lithosphere so we can assess if melt
388 generation would result from the current lithospheric thickness, which helps us determine if there
389 is sublithospheric melt beneath the RVP at present. Since the input shear wave seismic velocity
390 constraints (Emry et al., 2019) are static, we run the model until at least the first instance of peak
391 maximum melt generation ($\sim 2.5\%$ melt) which occurs at 1.6 Ma for models with excess
392 temperature in the sublithospheric mantle and the background sublithospheric mantle constrained

393 with $T_p = 1548$ K (red line; Figure 5). We therefore focus our interpretation of the TBC at 1.6 Ma
394 for the model with excess temperature in the sublithospheric mantle whose background
395 temperature is constrained with $T_p = 1548$ K, which is our best model. Figures 6A and 6B
396 respectively show 150 km and 250 km depth slices of sublithospheric mantle flow patterns
397 resulting from our numerical modeling of TBC at 1.6 Ma for our best model. Mantle upwelling
398 occurs where there are slow (negative) seismic velocity perturbations (Figure 2B; Emry et al.,
399 2019) which tend to be slowest at shallower depths beneath the thin lithosphere of the RVP.
400 Sublithospheric mantle downwelling occurs beneath the relatively thick lithosphere of the
401 surrounding cratons. At 150 km depth (Figure 6A), the sublithospheric mantle upwelling (~ 1
402 cm/yr) is focused beneath the RVP where the lithosphere is thin (~ 100 - 120 km) with a
403 characteristic radial horizontal mantle flow (~ 4 cm/yr). At 250 km depth (Figure 6B) there is a
404 zone of rapid mantle upwelling (~ 3 cm/yr) at the southwestern margin of the Tanzanian Craton,
405 that extends southeastward through the RVP to the northern segment of the Malawi Rift (Figure
406 6B). The mantle upwelling at 250 km depth has a horizontal flow pattern (~ 3 cm/yr) that is
407 characterized by a southwestward flow between and around the thick cratonic keels of the
408 Tanzanian and Bangweulu Cratons to the base of the lithosphere beneath the Malawi Rift. The
409 horizontal mantle flow stagnates beneath the RVP where there is rapid mantle upwelling (~ 2.5
410 cm/yr). This mantle flow pattern is consistent with earlier interpretations from seismic studies by

411 Grijalva et al. (2018).



412

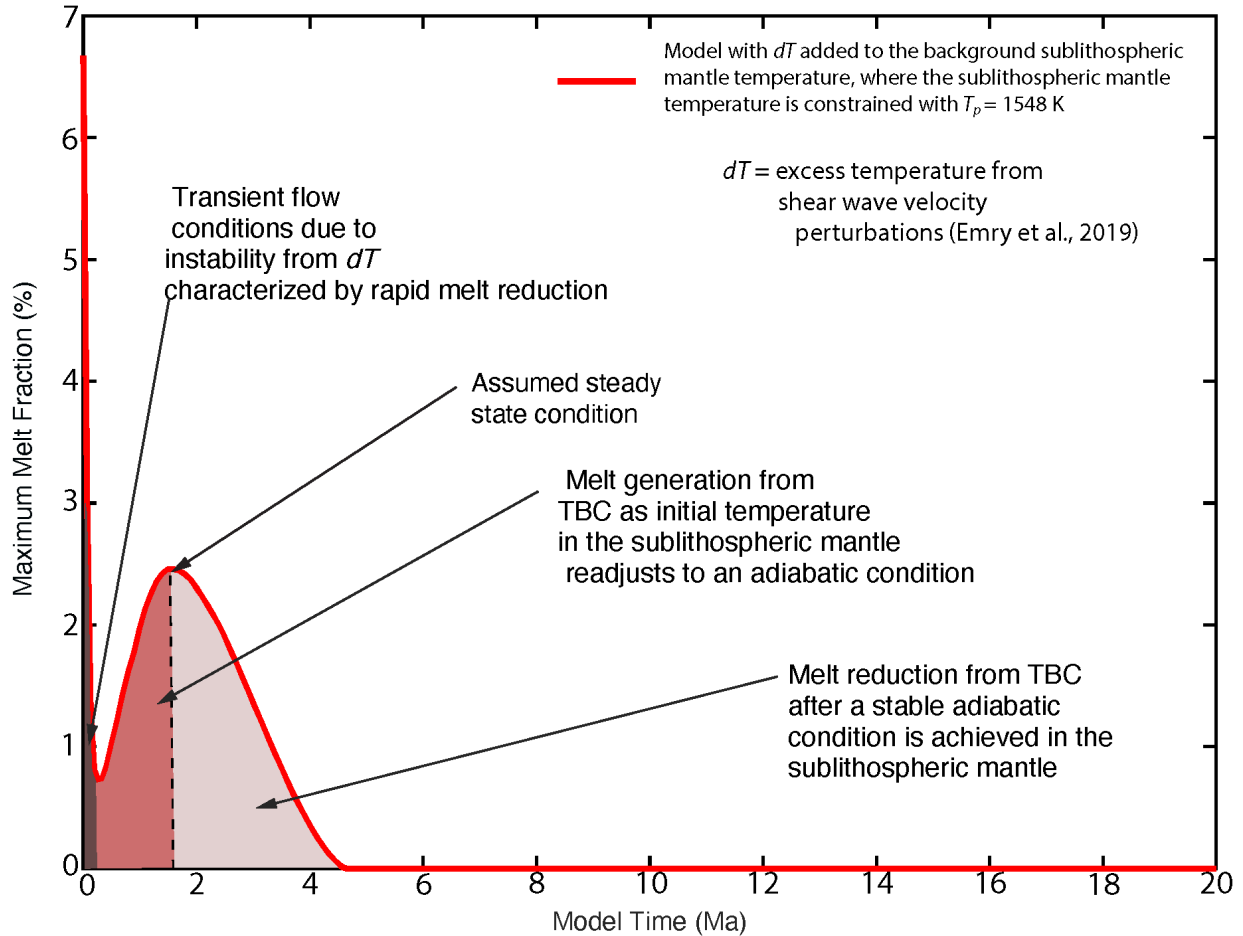
413 **Figure 6.** Depth slices showing tomography-based convection beneath the RVP and surrounding
 414 at (A) 150 km and (B) 250 km depth at 1.6 Ma for our best model, which is the model with
 415 excess temperature in the sublithospheric mantle whose background temperature is constrained
 416 with mantle potential temperature, $T_p = 1548$ K. The vertical flow (background colors) is
 417 overlain by the horizontal flow field (black arrows). Red triangles represent the RVP. Blue
 418 contours show lines of equal lithospheric thickness at 20 km intervals from Fishwick (2010).
 419 Black lines indicate the outline of rift lakes.

420

421 3.3 Melt Generation

422 We simulate tomography-based convection (TBC) and batch melting for 20 Ma (model
 423 time) to ensure that steady-state convection is achieved. We are not running the model forward in
 424 time to simulate lithospheric thinning, rather we are reducing computational error. The evolution
 425 of our best melting model, which is the model with excess sublithospheric mantle temperature

426 derived from shear wave velocity perturbations (Emry et al., 2019) and whose background
427 temperature is constrained with $T_p = 1548$ K (Figure 7) reveals two stages of melting. The first
428 stage ('the transient state'), occurs in the first 0.25 Ma of the model evolution beneath the RVP
429 and is characterized by an initial decompression melt of ~ 6.6 % melt. This 'transient state' of
430 melting arises from the initial conditions, which includes relatively thin lithosphere beneath the
431 RVP and excess sublithospheric mantle temperature. The endothermic melting process consumes
432 latent heat and there is adiabatic cooling of the upwelling mantle that rises to the melting region
433 (Njinju et al., 2021). The melting region thus experiences a net heat loss and progressively cools,
434 such that melting sustained by intrinsic density variations decreases rapidly from ~ 6.6 % at 0 Ma
435 to ~ 0.72 % melt at 0.25 Ma (Ballmer et al., 2007). We suggest the second melting phase (Figure
436 7) arises from TBC, which attains steady state at ~ 1.6 Ma after which the adiabatic gradients
437 within the active convection cell have adjusted from the initial values. During this second stage
438 of TBC-driven decompression melting, the melt fraction increases rapidly from 0.72 % at 0.25
439 Ma to a peak value of ~ 2.5 % at 1.6 Ma (Figure 7). Since the endothermic melting process
440 consumes latent heat, the melting region again experiences a net heat loss and progressively
441 cools, such that the melt fraction decreases from ~ 2.5 % at 1.6 Ma and ceases at 4.2 Ma.



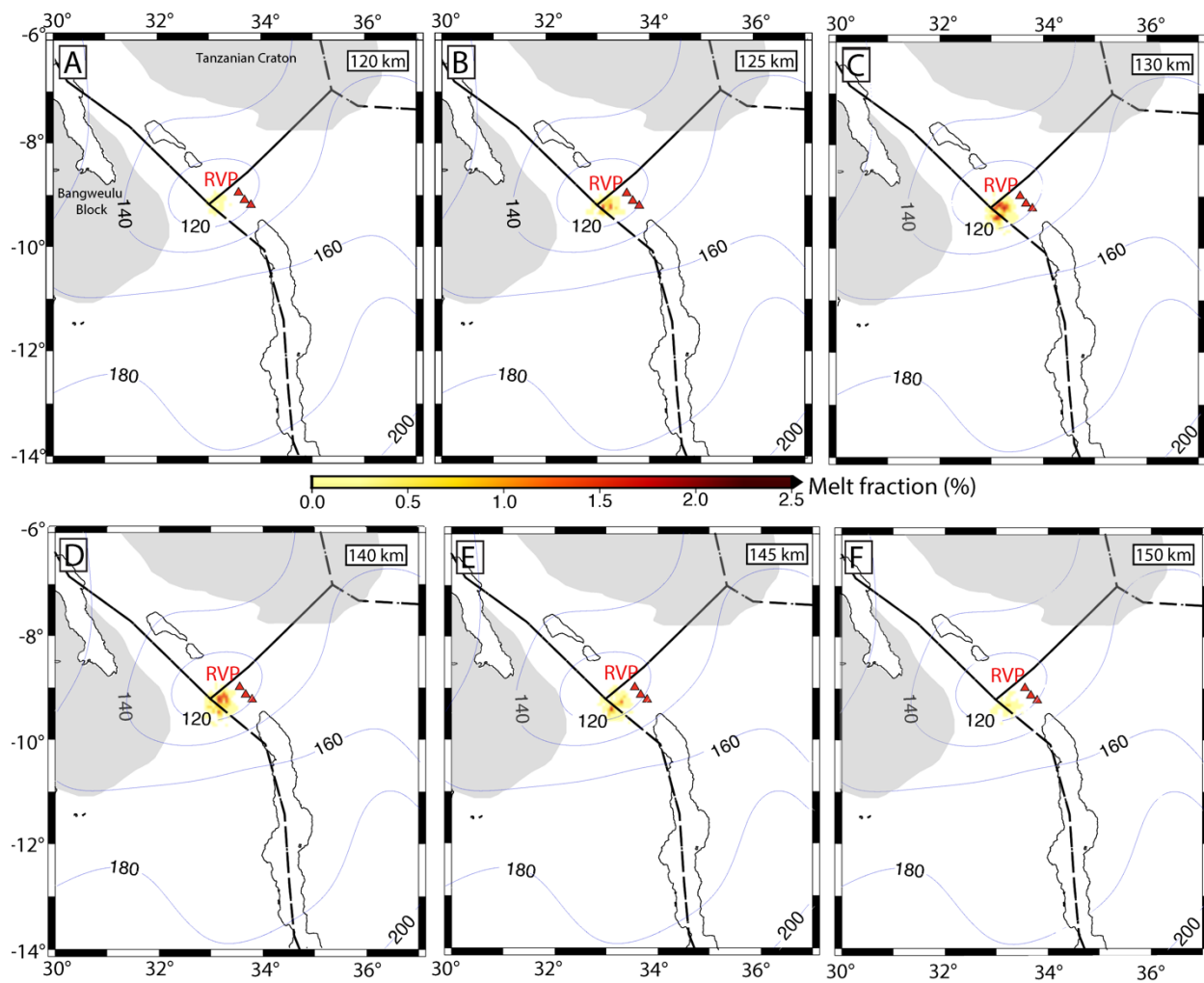
442

443 **Figure 7.** A plot of maximum melt fraction versus model time showing the evolution of melt for
 444 the model with excess temperature in the sublithospheric mantle whose background temperature
 445 is constrained with mantle potential temperature, $T_p = 1548$ K. Maximum melt generation due to
 446 tomography-based convection (TBC) is achieved at 1.6 Ma. The dark gray color (0 – 0.25 Ma)
 447 represents when tomography-based convection (TBC) is unstable and the initial decompression
 448 melt (~6.6 %) generated from the initial temperature conditions decreases rapidly to ~0.72 %
 449 melt at 0.25 Ma. The brown color (0.25 – 1.6 Ma) corresponds to melt generation from TBC
 450 with melt fractions increasing from 0.72 – 2.5%.

451

452 The melt model at 1.6 Ma for the model with excess temperature in the sublithospheric
 453 mantle whose background temperature is constrained with $T_p = 1548$ K (Figures 8A, B, C, D, E,
 454 and F) indicate that the melting region is focused beneath the thin lithosphere (~110 km) of the
 455 RVP particularly beneath the Mbeya triple junction, where there is a characteristic mantle

456 upwelling from TBC (Figure 6A). Depth slices of the melt model (Figures 8A, B, C, D, E, and F)
 457 indicate that melt generation due to TBC is restricted to depths of $\sim 115 - 155$ km beneath the
 458 RVP. At 120 km depth, the melt fraction is $< 0.5\%$ (Figure 8A), and at 125 km depth there are
 459 pockets of melt with melt fractions of $\sim 1\%$ at the center of the melting region (Figure 8B). The
 460 maximum melt fraction occurs at the center of the melting region (at depths of $\sim 130 - 140$ km)
 461 with melt fractions reaching $\sim 2\%$ (Figures 8C and 8D).



462

463 **Figure 8.** (A), (B), (C), (D), (E), and (F) show depth slices of melt fractions beneath the RVP at
 464 120 km, 125 km, 130 km, 140 km, 145 km, and 150 km depth respectively at 1.6 Ma for the
 465 model with excess temperature in the sublithospheric mantle whose background temperature is
 466 constrained with mantle potential temperature, $T_p = 1548$ K. Red triangles represent the RVP.
 467 Thin blue contours show lines of equal lithospheric thickness at 20 km intervals from Fishwick

468 (2010). Black lines indicate the outline of rift lakes. Black dotted lines delineate plate boundaries
469 from Stamps et al. (2008; 2021).
470

471 **4. Discussion**

472 4.1 Tomography-Based Convection versus Lithospheric Modulated Convection

473 We compare tomography-based convection (TBC) and lithospheric modulated
474 convection (LMC) beneath the RVP in order to better understand the influence of constraints of
475 the upper mantle structure on mantle flow, lithosphere-asthenosphere interactions, and melt
476 generation. Figures 9A and 9B respectively show TBC (model with excess temperature in the
477 sublithospheric mantle whose background temperature is constrained with $T_p = 1548$ K at Time
478 = 1.6 Ma) and LMC (model without tomography-based excess temperature in the sublithospheric
479 mantle and the background temperature is constrained with for $T_p = 1748$ K) with melt
480 generation beneath the RVP along profile AA'. And similarly, the TBC and LMC with melt
481 generation beneath the RVP along profile BB' are respectively shown in Figures 9C and 9D. The
482 main similarity between the TBC models (Figures 9A and 9C) and the LMC models (Figures 9B
483 and 9D) is that in both models, melt is generated beneath the thin lithosphere of the RVP with a
484 characteristic focused upwelling. However, melt generation from the LMC models occurs only
485 for highly elevated mantle potential temperatures ($T_p = 1748$ K) as observed in Njinju et al.
486 (2021).

487 The TBC models (Figures 9A and 9C), which has constraints on the upper mantle
488 structure from upper mantle velocity perturbations (Emry et al., 2019), show two regions of
489 mantle upwelling beneath the Tanzanian Craton, a region of upwelling beneath the southwestern
490 limit of the craton (Figure 9A), and another region of upwelling beneath the southeastern limit of
491 the craton (Figure 9C). The upwelling beneath the Tanzanian Craton is consistent with findings
492 of kimberlite deposits beneath the Tanzanian Craton and might be the source of the Igwisi Hills

493 Quaternary kimberlite (Dawson, 1994). These upwelling features are absent in the LMC models
494 (Figures 9B and 9D). The upper mantle structure beneath the Tanzanian Craton is characterized
495 by the presence of low velocity anomalies (Figure 2B; Emry et al., 2019) which translates to
496 excess temperature and density perturbations (buoyancy forces) that drive upwelling beneath the
497 craton.

498 The TBC model along profile BB' (Figure 9C) reveals a convection cell adjacent to the
499 southeastern margin of the Bangweulu Block that is not evident in the LMC model along profile
500 BB' (Figure 9D). This difference may be because the upper mantle constraints (Emry et al.,
501 2019) indicate that the base of the cratonic block is cold and the cratonic block might be thicker
502 than the estimates from Fishwick (2010).

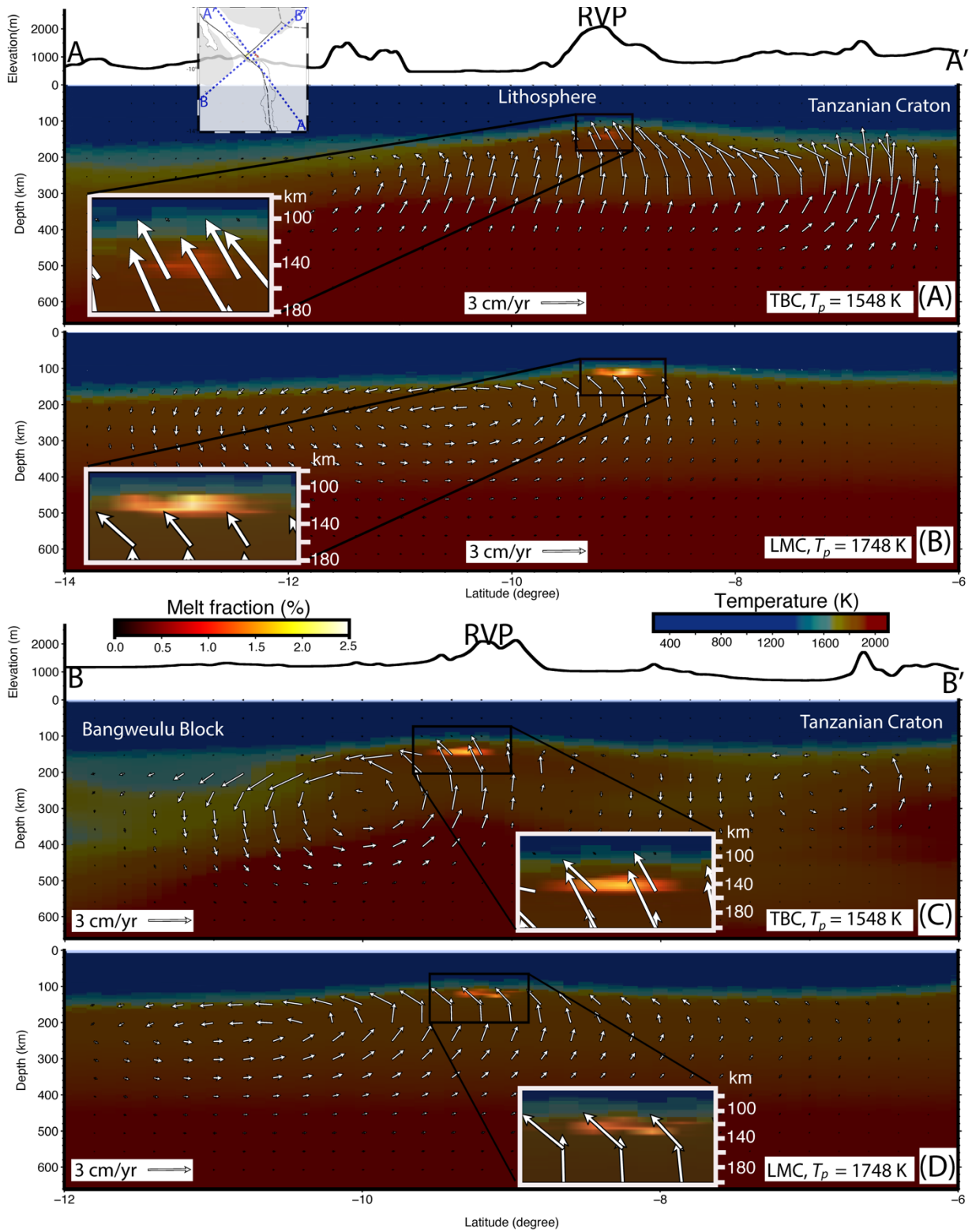
503 The LMC models (Figures 9B, and 9D) indicate lateral mantle flow at the lithosphere-
504 asthenosphere boundary over a longer interval than it is in the TBC models (Figures 9A, and
505 9C), which suggest that estimates of mantle traction (basal drag) from lithosphere-asthenosphere
506 interactions might be overestimated for mantle convections models constrained only by the
507 lithospheric structure (LMC) without considering the upper mantle structure.

508 4.2 Origin of Melt Beneath the Rungwe Volcanic Province and the Tectonic Implications

509 The most prominent feature in our model is the isolated region of sublithospheric mantle
510 upwelling and localized decompression melting due to TBC beneath the RVP at depths of ~115
511 – 155 km. The melt region is spatially consistent with a pronounced low velocity anomaly
512 beneath the RVP imaged from P-wave tomography (Grijalva et al., 2018; Yu et al., 2020). The
513 positive temperature anomalies (~ 250 K) in the sublithospheric mantle beneath the RVP inferred
514 from TBC (Figure 2C) suggests the presence of plume material beneath the RVP. The excess
515 temperature of plume material based on petrological studies is ~ 200 – 300 K (i.e., McKenzie

516 and O’Nions, 1991; Watson and McKenzie, 1991; Schilling, 1991; Herzberg and O’Hara, 2002;
517 Herzberg et al., 2007; Putirka, 2008). Petrological studies by Herzberg and Gazel (2009) suggest
518 excess temperature of ~100-250 K for hotspots in general. Thus, the low velocity anomaly
519 beneath the RVP may be a consequence of partial melts generated from plume material that is
520 deflected by the cratonic keels of the Tanzanian and Bangweulu Cratons and focuses beneath the
521 thin lithosphere of the RVP as earlier suggested by Grijalva et al. (2018). Upwelling and
522 decompression melt tend to focus beneath the thin lithosphere beneath the RVP, which suggests
523 that lateral variations in lithospheric thickness controls the localization of magmatism beneath
524 the RVP.

525 Geochemical studies of lava and tephra samples from the RVP by Hilton et al. (2011)
526 show significantly elevated $^3\text{He}/^4\text{He}$ ($>15 R_A$, where R_A is the helium isotopic ratio in air), far
527 exceeding typical upper mantle values. Such plume-like $^3\text{He}/^4\text{He}$ ratios, suggest that mantle
528 plume material contributes to the magmatism of the RVP. The high mantle potential temperature
529 (1693 – 1723 K; Rooney et al., 2012) and excess temperatures of ~250 K in the sublithospheric
530 mantle beneath the RVP are other indications of hot plume material beneath the RVP.



531

532

533 **Figure 9.** (A) Profile showing tomography-based convection (TBC) and melt generation
534 beneath the Rungwe Volcanic Province (RVP) (profile AA'; see inset map) at 1.6 Ma for the
535 model with excess temperature in the sublithospheric mantle whose background temperature is
536 constrained with $T_p = 1548$ K. (B) A profile of lithospheric modulated convection (LMC; model
537 without tomography-based excess temperature in the sublithospheric mantle and the background
538 temperature is constrained with $T_p = 1748$ K) and melt generation beneath the RVP along profile
539 AA'. (C) Same as (A) but for profile BB' (see inset map). (D) Same as (B) but for profile BB'.
540 The melting regions in Figures 9A, B, C and D are zoomed-in for better visibility and shown as
541 insets.
542

543 4.3 Model Limitations

544 Important factors that control the fraction of melt generated in a geodynamic model
545 includes the choice of parametrization for melting, which depends on temperature and pressure,
546 and the assumed composition of the source material. We use the parametrization of Katz et al.
547 (2003) for anhydrous peridotite. This parameterization is applicable for pressures less than 13
548 GPa. Although we use the melting parametrization of anhydrous peridotite (Katz et al., 2003), it
549 has been shown that high water content (Katz et al., 2003) and the use of recycled crustal
550 material (Sobolev et al., 2007, 2011) are also known to enhance melt production by several
551 percent. Thus, there is uncertainty in the computed melt fractions related to the constraints used
552 for melt generation and the composition of the mantle beneath the RVP.

553 Another simplification in this study is chemical homogeneity in the upper 660 km of the
554 mantle. We assume the seismic anomalies (Emry et al., 2019) are due to purely thermal effects in
555 an isochemical mantle convection framework. This approach has been successful in numerous
556 previous studies. For example, by representing seismic structures as mantle density and
557 buoyancy structures in a purely thermal, whole mantle convection model, geodynamic studies
558 have not only reproduced the Earth's geoid, but also provided constraints on the mantle viscosity
559 structure (e.g., Hager & Richards, 1989). In another case, by assuming thermal large low shear
560 velocity provinces (LLSVPs), Lithgow-Berterlloni and Silver (1998) explain dynamic

561 topography signatures which, like the geoid, has two prominent topographic highs over southeast
562 Africa and south Pacific. Despite successful implementations of isochemical mantle convection
563 models, the Earth's mantle is chemically heterogeneous as indicated by a rich variety of
564 geochemical signatures found in mantle derived basalts (i.e., Kunz et al., 1998; Rooney, 2020).
565 Thus, the observed low velocity anomaly beneath the RVP (Emry et al., 2019) might also be due
566 to compositional variations in the upper mantle in addition to thermal perturbations.

567 **5. Conclusions**

568 In this study, we develop a 3D thermomechanical model of tomography-based convection
569 (TBC) beneath the Rungwe Volcanic Province (RVP) that incorporates melt generation. We
570 assume an approximately conductive geotherm for the lithosphere, while for the sublithospheric
571 mantle, we use an adiabatic increase in temperature with additional temperature perturbations
572 derived from shear wave seismic velocity constraints. We assume a rigid lithosphere and use
573 non-Newtonian, porosity-dependent creep laws of anhydrous peridotite for sublithospheric
574 mantle convection. The seismic constraints indicate excess temperatures of ~ 250 K in the
575 sublithospheric mantle beneath the RVP suggesting the presence of a plume. Our TBC
576 simulation is characterized by an isolated sublithospheric mantle upwelling beneath the RVP,
577 which generates decompression melt ($\sim 2.5\%$ melt). Results of our TBC reveal some
578 characteristic mantle flow patterns (such as mantle upwelling beneath the Tanzanian Craton and
579 a corner flow adjacent to the southeastern margin of the Bangweulu Block) that are not evident
580 in LMC mantle flow models constrained by lithospheric thickness alone. Results of our TBC
581 suggest plume materials are the likely source of deep melt for the RVP which explains the high
582 $^3\text{He}/^4\text{He}$ values in the volcanic materials and the elevated mantle potential temperatures. Sharp
583 variations in the lithospheric thickness beneath the RVP and the surrounding cratons might

584 explain why the magmatism in the RVP is highly localized compared to the large igneous
585 provinces in the Eastern Branch of the East African Rift. We conclude that excess temperature
586 from plume material is necessary for melt generation beneath the RVP because passive
587 asthenospheric upwelling of ambient mantle will require higher-than-normal mantle potential
588 temperatures to generate melt. Further constraints on lithospheric structure and sublithospheric
589 structure of the upper mantle are required to better understand lithosphere-asthenosphere
590 interactions and deep melt generation.

591 **Acknowledgments**

592 This project was supported by the NSF EarthCube Integration grant #1740627. Most of the
593 figures in this paper were generated with Generic Mapping Tools V5.4.2 (Wessel et al., 2013).
594 We also created some of the figures with VISIT v2.9 developed by the Lawrence Livermore
595 National Laboratory. The lithospheric thickness file can be accessed from the BALTO Hyrax
596 server through the URL http://balto.opendap.org/opendap/lithosphere_thickness/. The mantle
597 flow model output files are available at the Open Science Framework repository with doi:
598 <https://doi.org/10.17605/OSF.IO/DY9Q4>. The ASPECT code and modified initial temperature,
599 initial composition and material models are available for open access through Zenodo at doi:
600 <https://zenodo.org/badge/latestdoi/381088620>. We thank the Computational Infrastructure for
601 Geodynamics for supporting the development of ASPECT, which is funded by National Science
602 Foundation Awards EAR-0949446 and EAR-1550901.

603

604 **References**

- 605 Asimow, P. D., & Stolper, E. M. (1999). Steady-state mantle–melt interactions in one dimension:
606 I. Equilibrium transport and melt focusing. *Journal of Petrology*, 40(3), 475-494.
- 607 Austermann, J., Mitrovica, J. X., Huybers, P., & Rovere, A. (2017). Detection of a dynamic
608 topography signal in last interglacial sea-level records. *Science Advances*, 3(7),
609 e1700457.
- 610 Bahame, G., Many, S., & Maboko, M. A. (2016). Age and geochemistry of coeval felsic
611 volcanism and plutonism in the Palaeoproterozoic Ndembera Group of southwestern

- 612 Tanzania: Constraints from SHRIMP U–Pb zircon and Sm–Nd data. *Precambrian*
613 *Research*, 272, 115-132.
- 614 Ballmer, M. D., Van Hunen, J., Ito, G., Tackley, P. J., & Bianco, T. A. (2007). Non-hotspot
615 volcano chains originating from small-scale sublithospheric convection. *Geophysical*
616 *Research Letters*, 34(23).
- 617 Bangerth, W., Dannberg, J., Gassmoeller, R., & Heister, T. (2018, June 24). Aspect V2.0.1.
618 Zenodo.<https://doi.org/10.5281/zenodo.1297145>.
- 619 Bangerth, W., Dannberg, J., Gassmoeller, R., Heister, T., & Others. (2018). ASPECT: Advanced
620 Solver for Problems in Earth’s ConvecTion, User Manual.
621 <https://doi.org/10.6084/m9.figshare.4865333>.
- 622 Becker, T. W. (2006). On the effect of temperature and strain-rate dependent viscosity on global
623 mantle flow, net rotation, and plate-driving forces. *Geophysical Journal International*,
624 167(2), 943-957.
- 625 Beauval, C., Yepes, H., Palacios, P., Segovia, M., Alvarado, A., Font, Y., ... & Vaca, S. (2013).
626 An earthquake catalog for seismic hazard assessment in Ecuador. *Bulletin of the*
627 *Seismological Society of America*, 103(2A), 773-786.
- 628 Castillo, P. R., Hilton, D. R., & Halldórsson, S. A. (2014). Trace element and Sr-Nd-Pb isotope
629 geochemistry of Rungwe Volcanic Province, Tanzania: implications for a superplume
630 source for East Africa Rift magmatism. *Frontiers in Earth Science*, 2, 21.
- 631 Class, C., Mesko, G. T., Plank, T. A., Boniface, N., & Many, S. (2018, December).
632 Thermobarometry of Silica-Undersaturated Rocks on the Example of Rungwe Volcanic

- 633 Province, Tanzania, East African Rift. In AGU Fall Meeting Abstracts (Vol. 2018, pp.
634 V53B-08).
- 635 Clauser, C., & Huenges, E. (1995). Thermal conductivity of rocks and minerals. *Rock physics*
636 *and phase relations: a handbook of physical constants*, 3, 105-126.
- 637 Conrad, C. P., & Behn, M. D. (2010). Constraints on lithosphere net rotation and asthenospheric
638 viscosity from global mantle flow models and seismic anisotropy. *Geochemistry,*
639 *Geophysics, Geosystems*, 11(5).
- 640 Conrad, C. P., & Lithgow-Bertelloni, C. (2006). Influence of continental roots and asthenosphere
641 on plate-mantle coupling. *Geophysical Research Letters*, 33(5).
- 642 Corti, G., van Wijk, J., Cloetingh, S., & Morley, C. K. (2007). Tectonic inheritance and
643 continental rift architecture: Numerical and analogue models of the East African Rift
644 system. *Tectonics*, 26(6).
- 645 Dannberg, J., Gassmüller, R., Grove, R., & Heister, T. (2019). A new formulation for coupled
646 magma/mantle dynamics. *Geophysical Journal International*, 219(1), 94-107.
- 647 Dannberg, J., & Heister, T. (2016). Compressible magma/mantle dynamics: 3-D, adaptive
648 simulations in ASPECT. *Geophysical Journal International*, 207(3), 1343-1366.
- 649 Dawson, J. B. (1994). Quaternary kimberlitic volcanism on the Tanzania Craton. *Contributions*
650 *to Mineralogy and Petrology*, 116(4), 473-485.
- 651 Ebinger, C., Deino, A., Drake, R., & Tesha, A. (1989). Chronology of volcanism and rift basin
652 propagation: Rungwe volcanic province, East Africa. *Journal of Geophysical Research:*
653 *Solid Earth*, 94(B11), 15785-15803.

- 654 Ebinger, C., Deino, A., Tesha, A., Becker, T., & Ring, U. (1993). Tectonic controls on rift basin
655 morphology: evolution of the Northern Malawi (Nyasa) Rift. *Journal of Geophysical*
656 *Research: Solid Earth*, 98(B10), 17821-17836.
- 657 Ebinger, C., Djomani, Y. P., Mbede, E., Foster, A., & Dawson, J. B. (1997). Rifting archaean
658 lithosphere: the eyasi-manyara-natron rifts, east africa. *Journal of the Geological Society*,
659 154(6), 947-960.
- 660 Emry, E. L., Shen, Y., Nyblade, A. A., Flinders, A., & Bao, X. (2019). Upper mantle Earth
661 structure in Africa from full-wave ambient noise tomography. *Geochemistry,*
662 *Geophysics, Geosystems*, 20(1), 120-147.
- 663 Faul, U. H., & Jackson, I. (2005). The seismological signature of temperature and grain size
664 variations in the upper mantle. *Earth and Planetary Science Letters*, 234(1-2), 119-134.
- 665 Fishwick, S. (2010). Surface wave tomography: imaging of the lithosphere–asthenosphere
666 boundary beneath central and southern Africa? *Lithos*, 120(1), 63-73.
- 667 Fontijn, K., Ernst, G. G., Elburg, M. A., Williamson, D., Abdallah, E., Kwelwa, S., ... & Jacobs,
668 P. (2010). Holocene explosive eruptions in the Rungwe volcanic province, Tanzania.
669 *Journal of volcanology and geothermal research*, 196(1-2), 91-110.
- 670 Fontijn, K., Williamson, D., Mbede, E., & Ernst, G. G. (2012). The Rungwe Volcanic Province,
671 Tanzania—A volcanological review. *Journal of African Earth Sciences*, 63, 12-31.
- 672 Fritz, H., Abdelsalam, M., Ali, K. A., Bingen, B., Collins, A. S., Fowler, A. R., ... & Viola, G.
673 (2013). Orogen styles in the East African Orogen: a review of the Neoproterozoic to
674 Cambrian tectonic evolution. *Journal of African Earth Sciences*, 86, 65-106.

- 675 Furman, T. (1995). Melting of metasomatized subcontinental lithosphere: undersaturated mafic
676 lavas from Rungwe, Tanzania. *Contributions to Mineralogy and Petrology*, 122(1-2), 97-
677 115.
- 678 Furman, T. (2007). Geochemistry of East African Rift basalts: an overview. *Journal of African*
679 *Earth Sciences*, 48(2-3), 147-160.
- 680 Ganbat, A., Tsujimori, T., Boniface, N., Pastor-Galán, D., Aoki, S., & Aoki, K. (2021). Crustal
681 evolution of the Paleoproterozoic Ubendian Belt (SW Tanzania) western margin: A
682 Central African Shield amalgamation tale. *Gondwana Research*, 91, 286-306.
- 683 Gassmöller, R., Dannberg, J., Bangerth, W., Heister, T., & Myhill, R. (2020). On formulations of
684 compressible mantle convection. *Geophysical Journal International*, 221(2), 1264-1280.
- 685 Goes, S., Armitage, J., Harmon, N., Smith, H., & Huisman, R. (2012). Low seismic velocities
686 below mid-ocean ridges: Attenuation versus melt retention. *Journal of Geophysical*
687 *Research: Solid Earth*, 117(B12).
- 688 Grijalva, A., Nyblade, A. A., Homman, K., Accardo, N. J., Gaherty, J. B., Ebinger, C. J., ... &
689 Mulibo, G. (2018). Seismic Evidence for Plume-and Craton-Influenced Upper Mantle
690 Structure Beneath the Northern Malawi Rift and the Rungwe Volcanic Province, East
691 Africa. *Geochemistry, Geophysics, Geosystems*, 19(10), 3980-3994.
- 692 Harkin, D. A. (1955). The Sarabwe Lava Flow, Kiejo, Rungwe District. *Tanganyika Notes and*
693 *Records*, 40, 20.
- 694 Hager, B. H., & Richards, M. A. (1989). Long-wavelength variations in Earth's geoid: physical
695 models and dynamical implications. *Philosophical Transactions of the Royal Society of*
696 *London. Series A, Mathematical and Physical Sciences*, 328(1599), 309-327.

- 697 Harkin, D. A. (1960). The Rungwe volcanics at the northern end of Lake Nyasa.
- 698 Heister, T., Dannberg, J., Gassmüller, R., & Bangerth, W. (2017). High accuracy mantle
699 convection simulation through modern numerical methods—II: realistic models and
700 problems. *Geophysical Journal International*, 210(2), 833-851.
- 701 Herzberg, C., Asimow, P. D., Arndt, N., Niu, Y., Leshner, C. M., Fitton, J. G., ... & Saunders, A.
702 D. (2007). Temperatures in ambient mantle and plumes: Constraints from basalts,
703 picrites, and komatiites. *Geochemistry, Geophysics, Geosystems*, 8(2).
- 704 Herzberg, C., & O'hara, M. J. (2002). Plume-associated ultramafic magmas of Phanerozoic age.
705 *Journal of Petrology*, 43(10), 1857-1883.
- 706 Herzberg, C., & Gazel, E. (2009). Petrological evidence for secular cooling in mantle plumes.
707 *Nature*, 458(7238), 619-622.
- 708 Hilbert-Wolf, H., Roberts, E., Downie, B., Mtelela, C., Stevens, N. J., & O'Connor, P. (2017).
709 Application of U–Pb detrital zircon geochronology to drill cuttings for age control in
710 hydrocarbon exploration wells: A case study from the Rukwa Rift Basin, Tanzania.
711 *AAPG Bulletin*, 101(2), 143-159.
- 712 Hilton, D. R., Halldórsson, S. A., Barry, P. H., Fischer, T. P., de Moor, J. M., Ramirez, C. J., ...
713 & Scarsi, P. (2011). Helium isotopes at Rungwe Volcanic Province, Tanzania, and the
714 origin of East African plateaux. *Geophysical Research Letters*, 38(21).
- 715 Hirth, G., & Kohlstedt, D. (2004). Rheology of the upper mantle and the mantle wedge: A view
716 from the experimentalists. *Inside the subduction Factory*, 138, 83-105.
- 717 Hudgins, T. R., Mukasa, S. B., Simon, A. C., Moore, G., & Barifaijo, E. (2015). Melt inclusion
718 evidence for CO₂-rich melts beneath the western branch of the East African Rift:

- 719 implications for long-term storage of volatiles in the deep lithospheric mantle.
720 *Contributions to Mineralogy and Petrology*, 169(5), 46.
- 721 Jadamec, M. A., & Billen, M. I. (2010). Reconciling surface plate motions with rapid three-
722 dimensional mantle flow around a slab edge. *Nature*, 465(7296), 338-341.
- 723 Jarvis, G. T., & Mckenzie, D. P. (1980). Convection in a compressible fluid with infinite Prandtl
724 number. *Journal of Fluid Mechanics*, 96(3), 515-583.
- 725 Katz, R. F., Spiegelman, M., & Langmuir, C. H. (2003). A new parameterization of hydrous
726 mantle melting. *Geochemistry, Geophysics, Geosystems*, 4(9).
- 727
- 728 Kennett, B. L., Engdahl, E. R., & Buland, R. (1995). Constraints on seismic velocities in the
729 Earth from traveltimes. *Geophysical Journal International*, 122(1), 108-124.
- 730 Kimani, C. N., Kasanzu, C. H., Tyne, R. L., Mtili, K. M., Byrne, D. J., Kazimoto, E. O., ... &
731 Barry, P. H. (2021). He, Ne, Ar and CO₂ systematics of the Rungwe Volcanic Province,
732 Tanzania: Implications for fluid source and dynamics. *Chemical Geology*, 586, 120584.
- 733 Koptev, A., Cloetingh, S., Gerya, T., Calais, E., & Leroy, S. (2018). Non-uniform splitting of a
734 single mantle plume by double cratonic roots: Insight into the origin of the central and
735 southern East African Rift System. *Terra Nova*, 30(2), 125-134.
- 736 Kunz, J., Staudacher, T., & Allegre, C. J. (1998). Plutonium-fission xenon found in Earth's
737 mantle. *Science*, 280(5365), 877-880.
- 738 LATIN, D., NORRY, M. J., & TARZEY, R. J. (1993). Magmatism in the Gregory Rift, East
739 Africa: evidence for melt generation by a plume. *Journal of Petrology*, 34(5), 1007-1027.

- 740 Lithgow-Bertelloni, C., & Silver, P. G. (1998). Dynamic topography, plate driving forces and the
741 African superswell. *Nature*, 395(6699), 269-272.
- 742 MacDonald, R., Rogers, N. W., Fitton, J. G., Black, S., & Smith, M. (2001). Plume–lithosphere
743 interactions in the generation of the basalts of the Kenya Rift, East Africa. *Journal of*
744 *Petrology*, 42(5), 877-900.
- 745 McKenzie, D. A. N., & Bickle, M. J. (1988). The volume and composition of melt generated by
746 extension of the lithosphere. *Journal of petrology*, 29(3), 625-679.
- 747 McKenzie, D. A. N., & O'nions, R. K. (1991). Partial melt distributions from inversion of rare
748 earth element concentrations. *Journal of Petrology*, 32(5), 1021-1091.
- 749 McKenzie, D. A. N., & O'NIONS, R. K. (1995). The source regions of ocean island basalts.
750 *Journal of petrology*, 36(1), 133-159.
- 751 Mei, S., Bai, W., Hiraga, T., & Kohlstedt, D. L. (2002). Influence of melt on the creep behavior
752 of olivine–basalt aggregates under hydrous conditions. *Earth and Planetary Science*
753 *Letters*, 201(3-4), 491-507.
- 754 Mesko, G., Class, C., Maqway, M., Boniface, N., Many, S., & Hemming, S. (2014). The
755 Timing of Early Magmatism and Extension in the Southern East African Rift: Tracking
756 Geochemical Source Variability with $^{40}\text{Ar}/^{39}\text{Ar}$ Geochronology at the Rungwe Volcanic
757 Province, SW Tanzania. Paper presented at the AGU Fall Meeting Abstracts, V51A-
758 4730.
- 759 Mesko, G. (2020). Magmatism at the Southern End of the East African Rift System: Origin and
760 Role During Early Stage Rifting (Doctoral dissertation, Columbia University).

- 761 Muirhead, J. D., Wright, L. J., & Scholz, C. A. (2019). Rift evolution in regions of low magma
762 input in East Africa. *Earth and Planetary Science Letters*, 506, 332-346.
- 763 Nielsen, T. K., & Hopper, J. R. (2002). Formation of volcanic rifted margins: Are temperature
764 anomalies required?. *Geophysical Research Letters*, 29(21), 18-1.
- 765 Njinju, E. A., Kolawole, F., Atekwana, E. A., Stamps, D. S., Atekwana, E. A., Abdelsalam, M.
766 G., & Mickus, K. L. (2019). Terrestrial heat flow in the Malawi Rifted Zone, East Africa:
767 Implications for tectono-thermal inheritance in continental rift basins. *Journal of*
768 *Volcanology and Geothermal Research*, 387, 106656.
- 769 Njinju, E. A., Atekwana, E. A., Stamps, D. S., Abdelsalam, M. G., Atekwana, E. A., Mickus, K.
770 L., ... & Nyalugwe, V. N. (2019). Lithospheric Structure of the Malawi Rift: Implications
771 for Magma-Poor Rifting Processes. *Tectonics*, 38(11), 3835-3853.
- 772 Njinju, E. A., Stamps, D. S., Neumiller, K., & Gallagher, J. (2021). Lithospheric Control of Melt
773 Generation Beneath the Rungwe Volcanic Province, East Africa: Implications for a
774 Plume Source. *Journal of Geophysical Research: Solid Earth*, 126(5), e2020JB020728.
- 775 O'Donnell, J. P., Selway, K., Nyblade, A. A., Brazier, R. A., Tahir, N. E., & Durrheim, R. J.
776 (2016). Thick lithosphere, deep crustal earthquakes and no melt: a triple challenge to
777 understanding extension in the western branch of the East African Rift. *Geophysical*
778 *Journal International*, 204(2), 985-998.
- 779 Purcell, P. G. (2018). Re-imagining and re-imaging the development of the East African Rift.
780 *Petroleum Geoscience*, 24(1), 21-40.
- 781 Putirka, K. (2008). Excess temperatures at ocean islands: Implications for mantle layering and
782 convection. *Geology*, 36(4), 283-286.

- 783 Rajaonarison, T. A., Stamps, D. S., Fishwick, S., Brune, S., Glerum, A., & Hu, J. (2020).
784 Numerical Modeling of Mantle Flow Beneath Madagascar to Constrain Upper Mantle
785 Rheology Beneath Continental Regions. *Journal of Geophysical Research. Solid Earth*,
786 125(2), Art-No.
- 787 Ribe, N. M. (1985). The generation and composition of partial melts in the earth's mantle. *Earth
788 and Planetary Science Letters*, 73(2-4), 361-376.
- 789 Roberts, E. M., Stevens, N. J., O'Connor, P. M., Dirks, P. H. G. M., Gottfried, M. D., Clyde, W.
790 C., ... & Hemming, S. (2012). Initiation of the western branch of the East African Rift
791 coeval with the eastern branch. *Nature Geoscience*, 5(4), 289-294.
- 792 Rogers, N., Macdonald, R., Fitton, J. G., George, R., Smith, M., & Barreiro, B. (2000). Two
793 mantle plumes beneath the East African rift system: Sr, Nd and Pb isotope evidence from
794 Kenya Rift basalts. *Earth and Planetary Science Letters*, 176(3-4), 387-400.
- 795 Rooney, T. O., Herzberg, C., & Bastow, I. D. (2012). Elevated mantle temperature beneath East
796 Africa. *Geology*, 40(1), 27-30.
- 797 Rooney, T. O. (2020). The Cenozoic magmatism of East Africa: part V—magma sources and
798 processes in the East African Rift. *Lithos*, 360, 105296.
- 799 Rosenthal, A., Foley, S. F., Pearson, D. G., Nowell, G. M., & Tappe, S. (2009). Petrogenesis of
800 strongly alkaline primitive volcanic rocks at the propagating tip of the western branch of
801 the East African Rift. *Earth and Planetary Science Letters*, 284(1-2), 236-248.
- 802 Schilling, J. G. (1991). Fluxes and excess temperatures of mantle plumes inferred from their
803 interaction with migrating mid-ocean ridges. *Nature*, 352(6334), 397-403.

- 804 Sobolev, A. V., Hofmann, A. W., Kuzmin, D. V., Yaxley, G. M., Arndt, N. T., Chung, S. L., ...
805 & Teklay, M. (2007). The amount of recycled crust in sources of mantle-derived melts.
806 *science*, 316(5823), 412-417.
- 807 Sobolev, S. V., Sobolev, A. V., Kuzmin, D. V., Krivolutskaya, N. A., Petrunin, A. G., Arndt, N.
808 T., ... & Vasiliev, Y. R. (2011). Linking mantle plumes, large igneous provinces and
809 environmental catastrophes. *Nature*, 477(7364), 312-316.
- 810 Stamps, D. S., Calais, E., Saria, E., Hartnady, C., Nocquet, J. M., Ebinger, C. J., & Fernandes, R.
811 M. (2008). A kinematic model for the East African Rift. *Geophysical Research Letters*,
812 35(5).
- 813 Stamps, D. S., Kreemer, C., Fernandes, R., Rajaonarison, T. A., & Rambolamanana, G. (2021).
814 Redefining East African Rift System kinematics. *Geology*, 49(2), 150-155.
- 815 Thiéblemont, D., Liégeois, J. P., Fernandez-Alonso, M., Ouabadi, A., Le Gall, B., Maury, R., ...
816 & Michard, A. (2016). Geological Map of Africa at 1: 10M scale. Geological Map.
817 CGMW-BRGM.
- 818 Van Wijk, J. W., Huisman, R. S., Ter Voorde, M., & Cloetingh, S. A. P. L. (2001). Melt
819 generation at volcanic continental margins: no need for a mantle plume?. *Geophysical*
820 *Research Letters*, 28(20), 3995-3998.
- 821 WATSON, S., & McKenzie, D. A. N. (1991). Melt generation by plumes: a study of Hawaiian
822 volcanism. *Journal of Petrology*, 32(3), 501-537.
- 823 Wessel, P., Smith, W. H., Scharroo, R., Luis, J., & Wobbe, F. (2013). Generic mapping tools:
824 improved version released. *Eos, Transactions American Geophysical Union*, 94(45), 409-
825 410.

- 826 White, R., & McKenzie, D. (1989). Magmatism at rift zones: the generation of volcanic
827 continental margins and flood basalts. *Journal of Geophysical Research: Solid Earth*,
828 94(B6), 7685-7729.
- 829 Yu, Y., Gao, S. S., Zhao, D., & Liu, K. H. (2020). Mantle Structure and Flow Beneath an Early-
830 Stage Continental Rift: Constraints From P Wave Anisotropic Tomography. *Tectonics*,
831 39(2), e2019TC005590.